Article:
Brain, M.J., Moya, S., Kincey, M.E. et al. (2021) Controls on post-seismic landslide behavior in brittle rocks. Journal of Geophysical Research: Earth Surface, 126 (9). e2021JF006242. ISSN: 2169-9003

https://doi.org/10.1029/2021jf006242

JGR Earth Surface

RESEARCH ARTICLE
10.1029/2021JF006242

Controls on Post-Seismic Landslide Behavior in Brittle Rocks

Matthew J. Brain[1], Sebastian Moya[2], Mark E. Kincey[1], Neil Tunstall[1], David N. Petley[3], and Sergio A. Sepúlveda[2,4]

[1]Department of Geography, Durham University, Lower Mountjoy, Durham, UK, [2]Departamento de Geología, Universidad de Chile, Santiago, Chile, [3]Department of Geography, University of Sheffield, Sheffield, UK, [4]Now at Department of Earth Sciences, Simon Fraser University, Burnaby, BC, Canada

Key Points:

- We used novel geotechnical testing to explore mechanisms that control post-seismic hillslope strength and rheology in brittle rocks
- The amplitude of dynamic loading can govern the nature of fractures and asperities formed, affecting subsequent shear strength and rheology
- The shear deformation mechanism mobilized determines whether post-seismic shear strength increases, decreases or remains unchanged

Supporting Information:

Supporting Information may be found in the online version of this article.

Correspondence to:

M. J. Brain,
matthew.brain@durham.ac.uk

Citation:

Brain, M. J., Moya, S., Kincey, M. E., Tunstall, N., Petley, D. N., & Sepúlveda, S. A. (2021). Controls on post-seismic landslide behavior in brittle rocks. *Journal of Geophysical Research: Earth Surface*, *126*, e2021JF006242. https://doi.org/10.1029/2021JF006242

Received 30 APR 2021
Accepted 31 AUG 2021

Abstract Earthquakes trigger widespread landsliding in tectonically active landscapes. The effects of strong ground shaking on hillslope stability persist into the post-seismic stage; rates of landsliding remain elevated in the years following an earthquake. The mechanisms that control the spatial pattern and rate of ongoing landsliding are poorly constrained, hindering our ability to reliably forecast how landscapes and landslide hazard evolve. To address this, we undertook a detailed geotechnical investigation in which we subjected representative rock samples to dynamic loading, simulating the effects of earthquake ground shaking on hillslopes of different configuration. Our results indicate that post-seismic hillslope strength is not an intrinsic rock property; rather, it responds to the amplitude of imposed dynamic loads and the degree of pre-existing shear surface formation within the rock. This path-dependent behavior results from differences in the character of fractures generated by dynamic loads of different amplitude, and the ways in which apertures are mobilized or degraded in subsequent (post-seismic) shearing. Sensitivity to dynamic loading amplitude is greater in shallow landslides in which shear surfaces are yet to fully form; such hillslopes can be strengthened or weakened by earthquake events, depending on their characteristics. In contrast, deeper landslides on steeper hillslopes in which shear surfaces have largely developed are less likely to display differences in behavior in response to dynamic loading because strain accumulation along pre-existing fractures is dominant. Our results demonstrate the need to consider path-dependent hillslope stability in numerical models used to forecast how landscapes respond to earthquakes and how post-seismic hazard evolves.

Plain Language Summary Landsliding is more common in the months and years after an earthquake. Our understanding of why this happens is limited but likely results from earthquake weakening of hillslopes. The mechanisms causing this weakening are difficult to assess at the landscape scale using satellite imagery. An alternative approach to improve our understanding of the controls on rock strength after an earthquake is to subject rock samples to seismic shaking in laboratory conditions. We used a custom-built apparatus to subject rock samples to pressure conditions typical of those experienced in shallow and deep-seated landslides. We simulated ground shaking of differing intensity to assess whether the rock was weaker or stronger after the shaking stopped. In simulated shallow landslides, ground shaking intensity affected how the sample cracked. Less intense shaking weakened the rock, implying it is more likely to fail following an earthquake. Conversely, more intense ground shaking strengthened the rock by creating a very uneven sliding surface, suggesting it is less likely to subsequently fail. Simulated deeper landslides on steeper hillslopes did not weaken, displaying less sensitivity to ground-shaking intensity. Our findings improve understanding of how hillslopes respond to seismic shaking, assisting forecasts of how landscapes and hazard develop after an earthquake.

1. Introduction

Seismic ground accelerations trigger large numbers of landslides in tectonically active, mountainous landscapes (Keefer, 1984; Parker et al., 2011; Roback et al., 2018). These coseismic slope failures, and the resultant release of large volumes of sediment into steep mountain catchments, have a significant effect on the geomorphic evolution of seismically active mountain regions (Croissant et al., 2019; Fan et al., 2018; Wang et al., 2015). Earthquake-triggered landslides can also result in considerable loss of life, damage to critical infrastructure and socio-economic disruption (Nowicki Jessee et al., 2020; Robinson et al., 2018).

It is therefore important to understand and, where possible, to forecast how hillslopes in seismically active landscapes respond to earthquake ground shaking (Malamud et al., 2004; Marc et al., 2016; Meunier et al., 2007).

The effects of earthquakes on hillslope stability are persistent; regional rates of landsliding can remain elevated above background levels over annual to decadal timescales following the mainshock event (Hovius et al., 2011; Koi et al., 2008; Marc et al., 2015; Zhang et al., 2016). The mechanisms responsible for this temporal pattern are poorly constrained (Rosser et al., 2021). Transient, elevated (i.e., above rainfall-normalized baseline conditions) rates of post-seismic landsliding are not ostensibly controlled by external seismic or meteorological forcing (Marc et al., 2015) and have instead been attributed to a combination of erosion of regolith weakened by earthquake ground shaking (Fan et al., 2018; Kincey et al., 2021; Lin et al., 2008; Wang et al., 2015), and/or recovery of hillslope strength in the post-seismic phase following initial disturbance and weakening during ground shaking (Leshchinsky et al., 2020; Marc et al., 2015, 2021). The mechanisms responsible for the latter are poorly constrained but have been postulated to result from a range of "healing" processes that include the re-establishment of plant-root cohesion (e.g., Jacoby, 1997; Yunus et al., 2020) and the reversal of dilation experienced during an earthquake as rock and soil masses settle and re-establish frictional contacts (e.g., Lawrence et al., 2009).

However, isolating the dominant mechanisms, and combinations thereof, that control the post-seismic evolution of hillslope strength is not straightforward across landscapes characterized by considerable variations in geomorphic setting, landslide type and morphology (Fan et al., 2018; Hu et al., 2018; Kincey et al., 2021), and substrate lithology, rheology, structure and stress history (Bontemps et al., 2020; Brain et al., 2017; Carey et al., 2017, 2021; Gischig et al., 2015; Hu et al., 2018; Lacroix et al., 2014; Samia et al., 2017a; Viles et al., 2018). Both mapped landslide inventories and local field studies reflect landscape and landform response to a specific earthquake event (Rosser et al., 2021). As such, use of limited inventories does not allow us to explore how hillslopes respond to different mainshock stress paths and, hence, the range of behavior that hillslopes could potentially exhibit in the post-seismic phase. This is important to establish because the specific nature of earthquake ground accelerations (duration, amplitude, and frequency content) can itself exert a key control on the evolution of substrate strength and rheology in the post-seismic phase (Parker et al., 2015; Sepúlveda et al., 2016). Furthermore, we lack detailed understanding of how hillslopes of different configuration deform in the post-seismic phase in response to earthquake ground shaking of differing character. Hillslope angle and landslide depth, for example, set the baseline (aseismic) shear stress, strain, and damage conditions (Bieniawski, 1967; Brain et al., 2014; Eberhardt et al., 1999; Martin & Chandler, 1994; Petley et al., 2005) that are subjected to ground accelerations during an earthquake. Different combinations of ground shaking intensity and hillslope configuration therefore have the potential to drive differences in post-seismic hillslope stability and/or behavior that are not captured in regional-scale mapping assessments (Marc et al., 2015).

The aim of this study is to determine how the intensity of ground shaking affects the post-seismic strength and rheology of rocks in hillslopes of different configuration and to constrain the mechanisms that cause any resultant variability. We used a novel geotechnical testing approach to subject samples of a single rock type to dynamic loads of varying amplitude to simulate differences in ground-shaking intensity in an earthquake mainshock. We then considered the effect of this dynamic loading on the subsequent deformation behavior of the rock, equivalent to the potential behavior of hillslopes in the post-seismic phase. We also explored if, how and why the baseline shear stress, a surrogate for hillslope angle, depth and, in turn, the degree of pre-seismic shear surface formation and damage, influenced the strength and rheology of the rock following dynamic loading, providing insight into the nature of hillslopes likely to experience elevated, or indeed reduced, susceptibility to post-seismic landsliding.

2. Rock Sampling Location

During the 2010 Mw 8.8 Maule earthquake, Chile (e.g., Delouis et al., 2010; Lorito et al., 2011), the Arauco Peninsula displayed elevated rates of landsliding, particularly in the sandstones and siltstones deposited in littoral settings during the late Pliocene and early Pleistocene (Escobar et al., 1982; Hackley et al., 2006; Melnick et al., 2009; Nielsen & Valdovinos, 2008; Serey et al., 2019). We obtained intact rock samples for

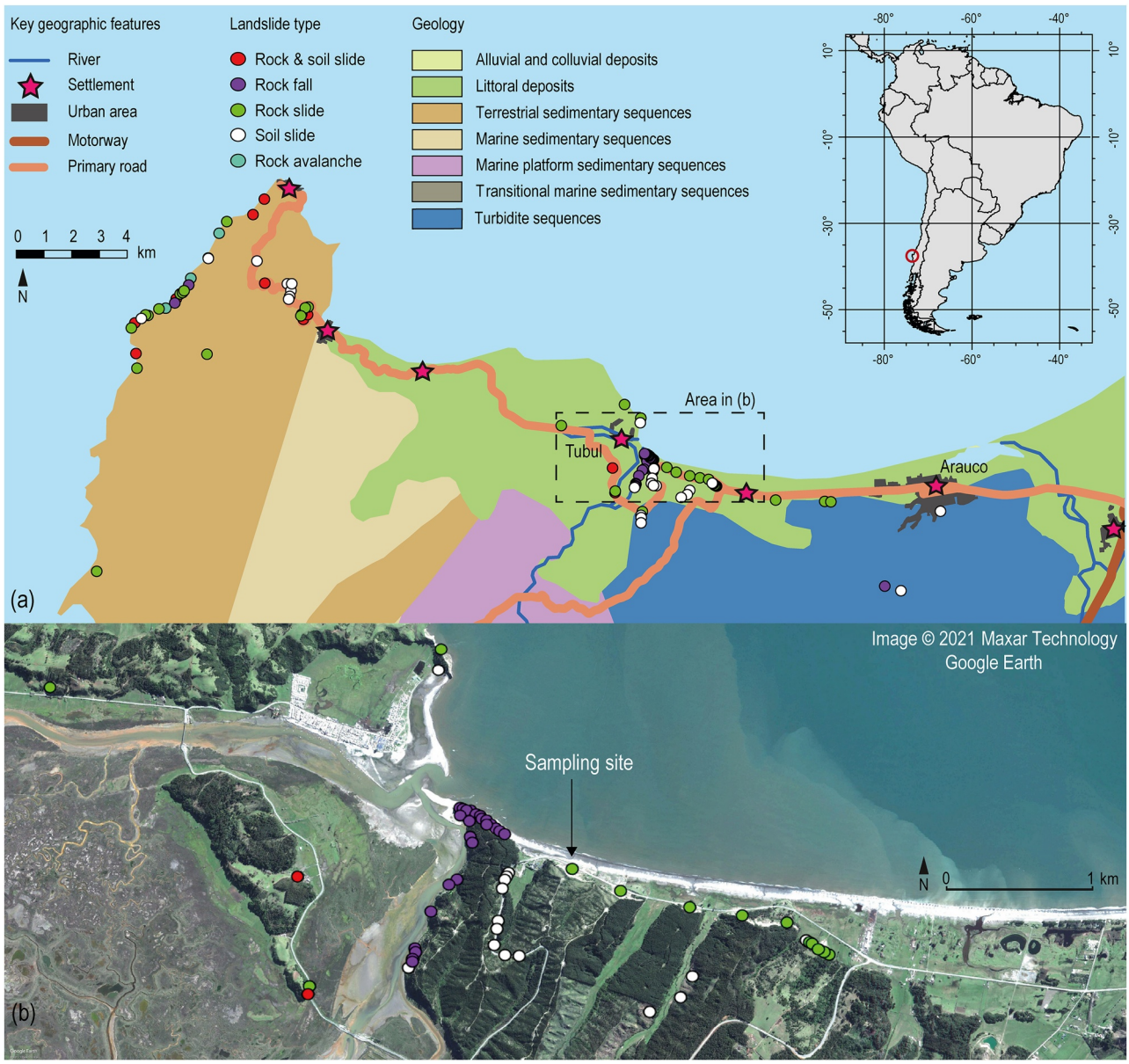

Figure 1. Rock sampling location in the Arauco Peninsula, Chile. (a) Summary of key geological and physiographic features within the study region. Mapped geology is based on Escobar et al. (1982) and Hackley et al. (2006). Inset: the location of the Arauco Peninsula region within South America is indicated by the red circle. (b) Location of the sampling location in the coastal outcrops of littoral deposits southeast of Tubul (Google Earth satellite image taken August 20, 2011). In both (a) and (b), the location and type of landslides triggered by the by the 2010 Maule earthquake were mapped and reported previously by Serey et al. (2019).

laboratory analysis from the accessible coastal outcrops of the Tubul Formation on the Arauco Peninsula (Figure 1). In our sampling region, the well-drained and largely massive rock slopes experienced disrupted translational landsliding during the 2010 Maule earthquake (Serey et al., 2019; Verdugo et al., 2010). Initial reconnaissance indicated the failure depth at the site was approximately 5–10 m. Our specific sampling location was selected such that unsheared, intact rock samples were sufficiently distant from locations where hillslope failure and coseismic damage occurred.

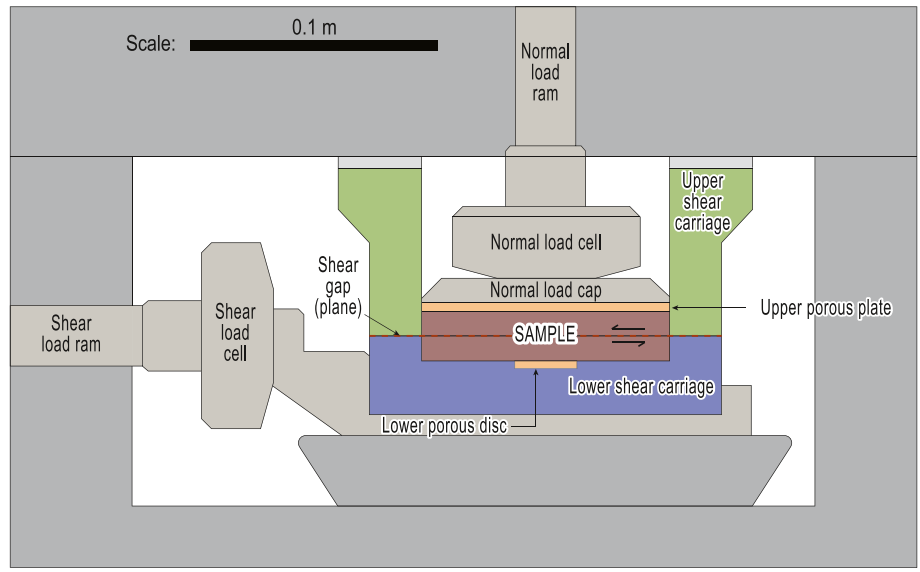

Figure 2. The internal components of the Dynamic Back-Pressured Shear box (DynBPS) apparatus (modified from Brain et al., 2015).

3. Methods

3.1. Sample Collection

We obtained unsheared and intact block samples (~0.3 × 0.3 × 0.3 m) of rock from hand-excavated (<1 m depth) pits at the base of the hillslope. Immediately following sampling, we sealed samples using plastic wrap to limit moisture loss and stored them in rigid containers to limit sample disturbance during transit. Samples were subsequently stored in refrigerated (~3°C) conditions to limit bacterial activity and, hence, sample modification prior to laboratory testing.

3.2. Rock Characterization

To classify and characterize the physical and index properties of the rock, we obtained sub-samples from the sampled blocks and ensured removal of a thin crust (~2–3 mm) of weathered near-surface material. Using standard methods, we determined the natural moisture content (by weight; $n = 9$), organic content by loss on ignition (550°C for 4 h; $n = 9$) and bulk density ($n = 13$ for intact samples) (Head, 2008; Head & Epps, 2011, 2014) of the sub-samples. We measured the point load strength, $I_{s(50)}$, of intact block samples ($n = 27$) using the method described by Franklin (1985). Using the point load data, we estimated the Unconfined Compressive Strength (σ_{UCS}) of the rock as 20 to 25 times the point load strength (Franklin, 1985).

We disaggregated an additional set of sub-samples using a pestle and mortar, using light pressure to prevent grain crushing. We determined the particle size distribution of the rock ($n = 7$) using a Beckman Coulter LS13320 Laser Diffraction Particle Size Analyzer, and classified the particle size data according to the scheme presented by Folk and Ward (1957) and supported by Blott and Pye (2001).

3.3. Geotechnical Laboratory Testing

3.3.1. Testing Apparatus

We undertook our geotechnical testing program using a Dynamic Back-Pressured Shear box (DynBPS) to subject rock samples (plan dimensions: 100 × 100 mm; depth: 20 mm; Figure 2) to direct shear, simulating conditions at a landslide shear surface (Brain et al., 2015, 2017; Carey et al., 2017). Use of direct shear testing to assess fracture and shear surface development in rocks under monotonic (e.g., Barla et al., 2010; Cresswell & Barton, 2003; Krsmanović, 1967; Lajtai, 1969a, 1969b; Yamasaki et al., 2016) and dynamic (e.g.,

Table 1
Summary of Direct Shear Test Conditions

	Sample type	Normal stress, σ_n (kPa)	Reference shear stress datum during dynamic loading, τ_{base} (kPa)	Dynamic shear stress amplitude, α_{dyn} (kPa)
Baseline monotonic tests				
1	Intact rock	50	–	–
2	Intact rock	50	–	–
3	Intact rock	50	–	–
4	Intact rock	100	–	–
5	Intact rock	100	–	–
6	Intact rock	150	–	–
7	Intact rock	150	–	–
8	Disaggregated grains	50	–	–
9	Disaggregated grains	100	–	–
10	Disaggregated grains	150	–	–
Dynamic tests				
11	Intact rock	50	47	20
12	Intact rock	50	47	40
13	Intact rock	50	172	20
14	Intact rock	50	172	40
15	Intact rock	50	219	20
16	Intact rock	50	219	40

Note. All samples were tested at natural moisture content. All monotonic shear was performed at a shear strain rate of 0.1% min^{-1}.

Asadollahi & Tonon, 2011; Fathi et al., 2016; Jafari et al., 2004; Qi et al., 2020; Sepúlveda et al., 2016) loading conditions is well established.

The DynBPS can apply axial (normal to the slope and shear surface) and horizontal (parallel to the slope and shear surface) loads to samples under monotonic or dynamic (≤5 Hz) conditions using either load or displacement control. All tests were undertaken in a climate-controlled laboratory at temperature of 21°C (±1°C) and a relative humidity of 50% (±5 percentage points).

We carefully trimmed sub-samples of our undisturbed blocks to the required dimensions of the cuboid shear box vessel, which is split into upper and lower sections (Figure 2). This vessel is mounted within the DynBPS. Normal stress, σ_n (kPa) is then applied to the sample via the normal load ram in a consolidation stage, simulating the effects of the weight of overlying rock at a landslide shear surface. To represent observed (i.e., drained and dry) field conditions at the time of sampling (see Selby, 1993; Whalley, 1991), all tests were undertaken with samples at their natural moisture content; we did not saturate them prior to or during testing. Hence, for these tests, we assumed that the normal stress applied to the samples is equivalent to normal effective stress (i.e., applied normal stress is directly transmitted to intergranular contacts within the sample during the test). To simulate shear, the DynBPS holds the upper section of the sample in place and displaces the lower section laterally along the "shear gap" (2.1 mm height) between these sections at the approximate vertical mid-point of the sample.

We completed a total of 16 direct shear tests (10 monotonic "baseline" tests and six dynamic tests; Table 1). During all tests, we recorded normal stress, shear stress (τ, kPa), normal strain ($\varepsilon_{n,}$ %), and shear strain ($\varepsilon_{s,}$ %). For all direct shear tests (Table 1), strain values were calculated relative to original sample dimensions prior to consolidation. Positive normal strain values indicate sample compression relative to initial sample dimensions, whereas negative values indicate dilation relative to initial sample geometry. During consolidation and monotonic shear stages, we specified a data sampling frequency of 0.1 Hz. During dynamic

tests, the data sampling frequency was 100 Hz. On completion of each test, we carefully documented the nature of failure in the samples, paying particular attention to the degree and configuration of fracturing, the nature of the shear surface, and the absence or presence of disaggregated rock particles. We interpreted data and observations for each test to develop understanding of the mechanisms of failure and, hence, an explanation of any differences in behavior between each test.

3.3.2. Characterizing Baseline Direct Shear Behavior

The first stage in our laboratory testing program involved characterization of the monotonic shear behavior of intact samples to constrain the "baseline" condition against which the effects of dynamic loading on the strength, failure mechanisms and rheology of the rock could be compared. We selected monotonic direct shear behavior to represent our baseline condition because the strength parameters obtained from these tests (cohesion and friction angle) are used in calculations in the static Factor of Safety that is integral to many pseudo-dynamic assessments of slope stability during earthquakes (e.g., Jibson, 1993; Newmark, 1965). In our baseline tests, we used shear strain controlled monotonic direct shear tests following standard methods (Head & Epps, 2011, 2014; Muralha et al., 2014) at a shear strain rate of 0.1% min^{-1}. To investigate the effects of overburden thickness/depth of the shear plane on the behavior of intact rock samples, we carried out seven tests under normal stress values of 50 kPa ($n = 3$), 100 kPa ($n = 2$), and 150 kPa ($n = 2$). This range of normal stress values is equivalent to those experienced by a range of landslides depths and hillslope angles. The additional test at a normal stress of 50 kPa was carried out to better constrain variability in behavior, since this is the normal stress used during the dynamic testing stages (following Barbero et al., 1996, the effects of dynamic loading are likely to be more pronounced at lower normal stresses).

We undertook an additional three tests on disaggregated rock samples at normal stress values of 50 kPa ($n = 1$), 100 kPa ($n = 1$), and 150 kPa ($n = 1$) following standard methods (e.g., Carter, 1990; Head, 2008). These three tests were undertaken to constrain the fully softened behavior of the rock, equivalent to conditions in which cohesion has been lost.

We defined three key failure envelopes (best estimate ± one standard error) using least squares linear regression: intact rock peak strength, residual strength (calculated in each test as the mean shear stress for shear strain values between 15% and 18% in monotonic tests) and fully softened strength, obtained from the direct shear tests on disaggregated rock.

To permit assessment of the effects of dynamic loading on direct shear behavior, we specified "peak" and "residual" ranges of shear stress, defined by the minimum and maximum values of peak and residual strength observed in the baseline direct shear tests undertaken at a normal stress of 50 kPa. These strength envelopes are similar to the modeled failure envelope strength predictions at a normal stress of 50 kPa but cover a broader baseline strength range against which post-dynamic shear behavior can be compared. This broader definition of baseline conditions is important to consider; any differences in behavior attributed to dynamic loading must at least exceed variability in behavior observed in our baseline data set.

3.3.3. Direct Shear Behavior Under Dynamic Loading

For each dynamic test ($n = 6$), we first applied a normal stress of 50 kPa to each intact rock sample. We selected 50 kPa to represent typical normal stress conditions experienced in shallow (<5 m depth) landslides on hillslopes of 30–40° that characteristically fail in response to earthquake ground accelerations (Kincey et al., 2021; Lin et al., 2008; Saito et al., 2018; Tanyaş et al., 2017). Holding normal stress constant, we then increased shear stress (shear strain rate of 0.1% min^{-1}) to a specific reference datum (τ_{base}) to simulate the aseismic in situ shear stress in hillslopes of different configuration (hillslope angle and landslide depth) and corresponding variations in the degree of shear surface formation and/or accumulated damage with the sample (Petley et al., 2005). To do so, we defined three τ_{base} values on the basis of established crack initiation and propagation thresholds for brittle rock in unconfined compression (in the absence of equivalent thresholds for direct shear) (see e.g., Cai et al., 2004; Eberhardt et al., 1999), refined based on the results and observations from our baseline tests. Since we were interested in the effects of dynamic loading on unfailed hillslopes (following Sepúlveda et al., 2016), τ_{base} values were specified relative to the peak strength values observed in monotonic conditions at a normal stress of 50 kPa. This range of stress states allowed

us to explore how hillslopes of different configuration respond to dynamic loading events. The lowest τ_{base} was equivalent to 20% of the peak shear strength, indicative of hillslopes that have experienced limited shear surface formation and accumulated damage, below typical crack initiation thresholds in brittle rocks (typically 30%–50% of peak strength; Cai et al., 2004). The stress conditions we specify for this τ_{base} (Section 4.3.1) are broadly representative of shallow (vertical depth to failure surface, z, ≤5 m) landslides occurring on hillslope angles, β, of 30°–40°, typical of those prone to failure during earthquakes (Fan et al., 2018; Kincey et al., 2021; Lin et al., 2008; Marc et al., 2016; Saito et al., 2018). The intermediate τ_{base} was 75% of peak strength, at the likely onset of shear fracture coalescence (typically 70%–90%) and indicative of deeper landslides in steeper, saturated hillslopes ($z \approx$ 20–25 m; $\beta \approx$ 35°–40°). The upper τ_{base} was 95% of peak strength and represents effective stress conditions equivalent to those experienced in deeper-seated landslides ($z \approx$ 30–35 m; $\beta \approx$ 35°–40°) in which shear fractures have largely coalesced to form a continuous shear surface that is prone to progressive, creep-type and/or episodic deformation in response to rainfall events or seismic forcing (e.g., Bontemps et al., 2020; Lacroix et al., 2014; Petley & Allison, 1997).

For each τ_{base}, we completed two dynamic tests to investigate the effect of differing dynamic shear stress amplitude (α_{dyn}) on direct shear behavior to simulate "low" (±20 kPa) and "high" (±40 kPa) intensity seismic events. Assuming rock bulk density values typical of our study site (Section 4.1 below), a landslide depth of ~5 m and a hillslope angle of 35°, these dynamic shear stresses are equivalent to horizontal ground accelerations of ~0.33 and ~0.66 g, respectively (following Hadj-Hamou & Kavazanjian, 1985). In deeper landslides (β = 35°), equivalent horizontal ground accelerations are ~0.1–~0.2 g ($z \approx$ 20 m) and ~0.06–~0.12 g ($z \approx$ 30 m).

For the dynamic shear stages, we controlled shear stress (rather than strain) to permit shear strain to accumulate in response to ground shaking (see Brain et al., 2015 for a more detailed rationale); shear strain control under dynamic conditions would not simulate or permit this behavior.

For each dynamic stage, we used sinusoidal waveforms (see Brain et al., 2015; Christakos, 2003 for a summary of the rationale) and a frequency of 1 Hz, reflecting the dominant shaking frequency recorded at several sites during the 2010 Maule earthquake (Elnashai et al., 2010). Each dynamic stage lasted 30 s, consistent with a range of observations of the duration of strong ground motions resulting from earthquakes of varying magnitude (Salmon et al., 1992; Trifunac & Brady, 1975). Specified normal stress remained at 50 kPa throughout each dynamic testing stage. Following completion of the dynamic stage, we continued monotonic shearing of the sample (σ_n = 50 kPa; shear strain rate of 0.1% min^{-1}) until maximum shear displacement was achieved. We then compared the post-dynamic behavior of the sample to our baseline behavior to determine if any changes in strength and rheology had resulted from dynamic loading.

3.4. Quantitative Shear Surface Characterization

Following completion of the initial set of geotechnical tests, we undertook two additional direct shear tests to characterize the shear surface of failed materials under different scenarios to improve our understanding of mechanisms responsible for differences in observed behavior. The first was a repeat of Tests 1, 2, and 3 (σ_n = 50 kPa, monotonic shear) and the second was a repeat of Tests 6 and 7 (σ_n = 150 kPa, monotonic shear). However, each test was stopped following exceedance of peak shear stress and the DynBPS was disassembled to allow capture of the initial failure surface resulting from initial fracture. We then quantitatively analyzed the post-failure form of the lower shear surface within the DynBPS apparatus using three-dimensional reconstructions using structure-from-motion (SfM) photogrammetry (e.g., Anderson et al., 2019; Swirad et al., 2019). For each sample, we captured ~75 photographs from multiple view angles using a Nikon Coolpix P7700 (12 megapixel) digital camera (6 mm focal length with automatic exposure). We kept light conditions constant during photograph capture using two tripod-mounted spotlights with diffuse lighting umbrellas. Following Carbonneau and Dietrich (2017) and Fonstad et al. (2013), we used convergent camera positions at ~45° azimuth interval to capture images at heights ranging between ~0.1 and 1 m above the sample. We also obtained nadir images at each height interval. Average ground pixel resolution of the resulting photographs was 0.11 mm.

Initial processing of the SfM data was conducted using Agisoft Photoscan Professional v.1.4.3, with the initial photo alignment yielding >62,000 image tie points for each model. We accurately scaled the model

Table 2
Physical Properties of the Tubul Formation Rock Tested

	Particle size			Natural moisture content (%)	Loss on ignition (%)	Bulk density (g cm^{-3})			Disaggregated bulk density (g cm^{-3})
	Sand (%)	Silt (%)	Clay (%)			Monotonic tests	Dynamic tests	All tests	
Mean	50.9	46.2	2.9	3.78	1.65	1.48	1.47	1.48	1.14
Standard deviation	–	–	–	1.70	0.11	–	–	0.02	–
Minimum	41.6	35.3	1.9	2.35	1.53	1.45	1.45	1.45	1.10
Maximum	62.8	54.7	3.7	6.77	1.86	1.52	1.50	1.52	1.16
Number of samples	7	7	7	9	9	7	6	13	3

using a local coordinate system based on the known dimensions of the DynBPS, using the approach recommended by James et al. (2017). The average root mean squared error (RMSE) for the XYZ georeferencing was 0.33 mm. We meshed and converted the final dense point clouds (an average of 6.65 million points) into 0.1 mm-resolution orthophotographs and 0.2 mm-resolution digital elevation models (DEMs), permitting the extraction of topographic profiles along the shear surface to better characterize surface planarity and/or roughness. Further details of the SfM workflow and associated errors (in accordance with James et al., 2019) are included within the Supporting Information S1.

4. Results

4.1. Rock Type and Physical Properties

The rock samples obtained from the Tubul Formation were greyish yellow/yellowish gray (following Munsell, 2009), with pale yellowish orange sections resulting from iron enrichment. The rock did not display any obvious fissility.

The physical properties of the rock are displayed in Table 2. The rock was composed primarily of sand- (mean = 50.9%) and silt- (mean = 46.2%) sized grains, with low clay content (mean = 2.9%). Following Folk and Ward (1957), the rock can be classified as a very fine sandstone/very coarse siltstone. Natural moisture and organic content by loss on ignition were low (mean values of 3.78% and 1.65% respectively). The mean bulk density of intact sub-samples was 1.48 g cm^{-3}, with no ostensible differences in bulk density between samples used in monotonic (mean = 1.48 g cm^{-3}) and dynamic (mean = 1.47 g cm^{-3}) tests. Disaggregated samples tested in direct shear displayed a mean bulk density of 1.14 g cm^{-3} prior to consolidation during shear box testing.

Point load test results are summarized in Table 3. Samples displayed a mean point load strength, $I_{s(50)}$, of 0.13 ± 0.03 MPa (one standard deviation), yielding estimated mean σ_{UCS} values between 2.64 ± 0.72 and 3.31 ± 0.72 MPa. Following ISRM (1981), the rock can be classified as "very weak."

Table 3
Summary of Results for Point Load Tests Undertaken on the Tubul Formation Rock Tested

		Estimated unconfined compressive strength (MPa)	
	Point load strength, $I_{s(50)}$, (MPa)	Lower estimate ($I_{s(50)} \times 20$)	Upper estimate ($I_{s(50)} \times 25$)
Mean	0.13	2.64	3.31
Standard deviation	0.03	0.72	0.72
Minimum	0.04	0.89	1.11
Maximum	0.18	3.55	4.43
Number of samples	25[a]	–	–

[a]Following Franklin (1985), the highest and lowest recorded values were discarded from analysis.

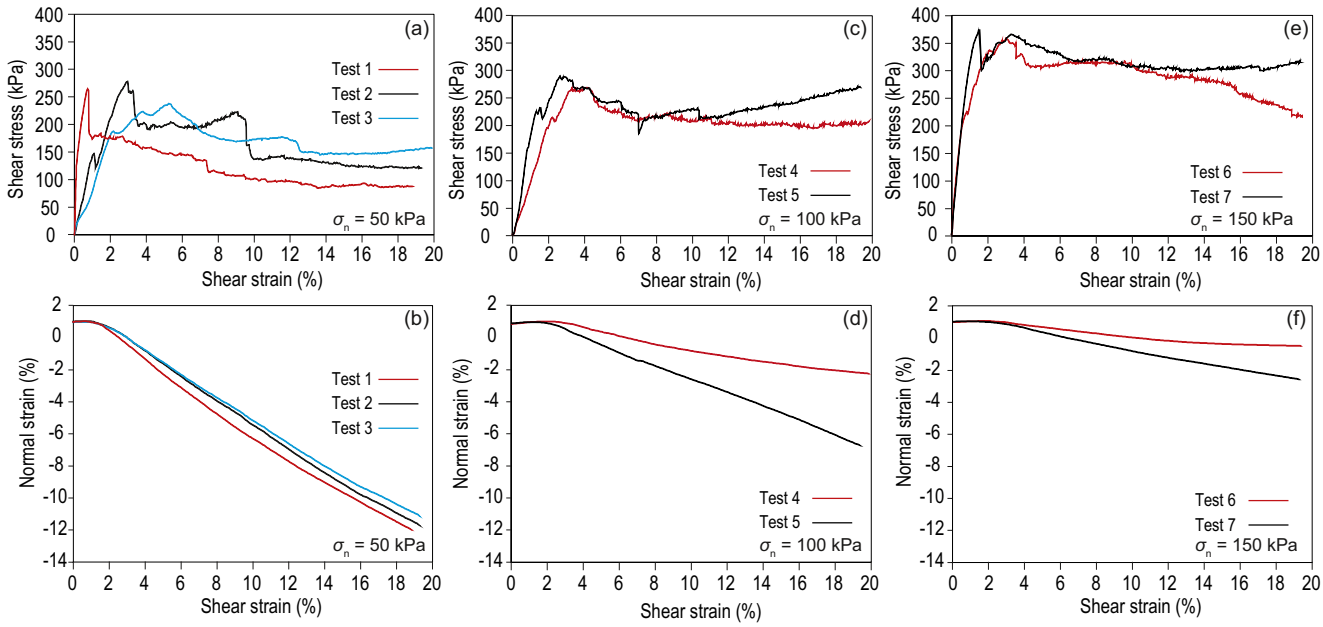

Figure 3. Shear stress-strain (a, c, and e) and normal strain (b, d, and e) behavior of intact rock samples subjected to monotonic direct shear at normal stresses of 50 kPa (a and b), 100 kPa (c and d) and 150 kPa (e and f).

4.2. Baseline Direct Shear Behavior

4.2.1. Monotonic Tests at $\sigma_n = 50$ kPa

Stress-strain curves for intact rock samples tested in monotonic direct shear are displayed in Figure 3. For tests 1, 2, and 3 ($\sigma_n = 50$ kPa), the rock displayed a brittle-ductile rheology characterized by an increase to a peak shear stress (267.8, 278.1, and 237.0 kPa) followed by a reduction to a residual strength condition (~90.0, ~121.9, and ~146.6 kPa) (Figure 3a). Pre-peak behavior varied between samples; peak shear stress values were achieved at shear strain values of 0.75%, 3.0%, and 5.4%. The nature of the reduction in shear stress following exceedance of peak shear stress varied between tests, occurring through a combination of (a) relatively "smooth" and gradual decreases in shear stress as shear strain accumulated (reductions of ~40–80 kPa over shear strain increments of 4%–5%); and (b) more brittle stress drops over shorter shear strain increments (reductions of 20–80 kPa over shear strain increments of 0.1%–0.5%). The onset of apparent residual strength occurred at shear strains between approximately 13% and 14%.

Volumetric strain curves for these tests showed greater consistency between samples (Figure 3b). Following normal strains resulting from consolidation (~1%), the samples displayed limited normal strain accumulation at shear strain values < 0.9%, before dilating at largely constant rate. We observed normal strains of approximately −11%–−12% at the end of each test.

Following completion of the tests, samples were heavily fractured and dilated, with multiple sub-vertical cracks extending from the shear plane to the top and base of the sample (Figure 4a) and all apertures contained shear gouge (smaller rock fragments and disaggregated grains).

4.2.2. Monotonic Tests at $\sigma_n = 100$ kPa

Intact samples tested under a normal stress of 100 kPa displayed peak shear stress values of 269.2 and 289.3 kPa and residual shear stress values of 198.2 and 247.4 kPa (Figure 3c). Samples displayed a brittle-ductile rheology characterized by a gradual reduction from peak to residual strength that was punctuated by brittle stress drops of ~10–20 kPa and was largely complete by a shear strain of 8%. In test 5, the sample continued to increase in strength as strain proceeded ($\varepsilon_s > 10\%$; Figure 3e). This sample showed greater dilatancy, reaching a normal strain value of −6.75% at the end of the test. In contrast, the sample in test 4 dilated less (normal strain of −2.23% at the end of the test).

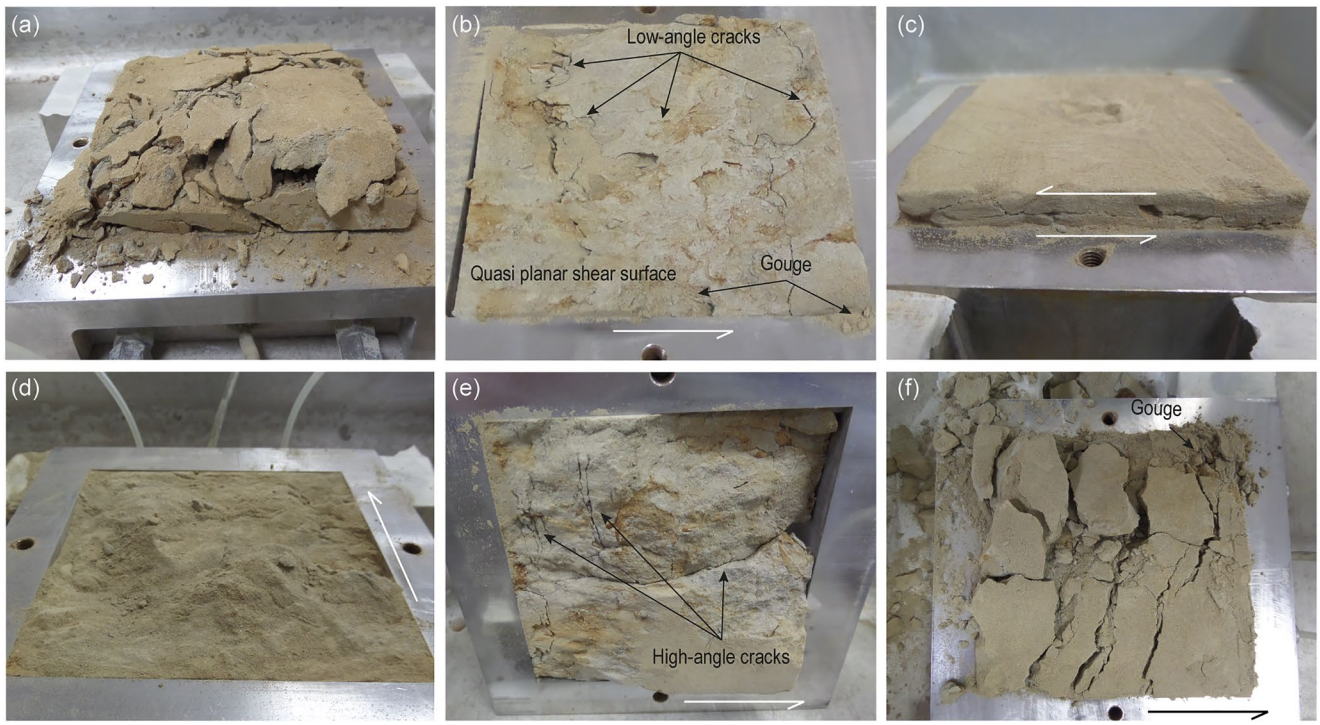

Figure 4. Post-test photographs of samples demonstrating key characteristics of shear surfaces resulting from differences in shear and deformation mechanisms in response to variations in normal stress, accumulated shear strain and/or dynamic loading amplitude. (a) Test 1 (σ_n = 50 kPa) showing high sample dilation, high angle fracturing and gouge formation. (b) Test 4 (σ_n = 100 kPa) showing low angle cracking throughout the lower section of sheared rock and a relatively planar shear surface focused at the shear gap. (c) Test 6 (σ_n = 150 kPa) showing coherent upper and lower shear blocks, limited shear-oblique cracking and a largely planar shear surface. (d) Test 11 (σ_n = 50 kPa, τ_{base} = 47 kPa, α_{dyn} = 20 kPa) showing a degraded/smoothed "Type B" failure surface. (e) Test 13 (σ_n = 50 kPa, τ_{base} = 172 kPa, α_{dyn} = 20 kPa) showing a degraded/smoothed "Type A" failure surface, with evidence of high angle cracks that were not fully mobilized to accommodate shear. (f) Test 14 (σ_n = 50 kPa, τ_{base} = 172 kPa, α_{dyn} = 40 kPa) displaying several high angle fractures extending throughout height of the sample and a gouge-filled shear band along the shear gap.

Following testing, samples were visibly less dilated and more coherent (Figure 4b) than those sheared under a normal stress of 50 kPa. Upper and lower blocks displayed considerably reduced fracture density. Failure was more evidently concentrated at the approximate vertical mid-point of the sample (i.e., focused at the shear gap, resulting in a band of shear gouge), though a single discrete and fully planar shear surface did not form. Instead, shear was accommodated along multiple low angle fractures extended throughout the sample both above and below the shear gap, but these fractures did not all extend to the top and base of the sample.

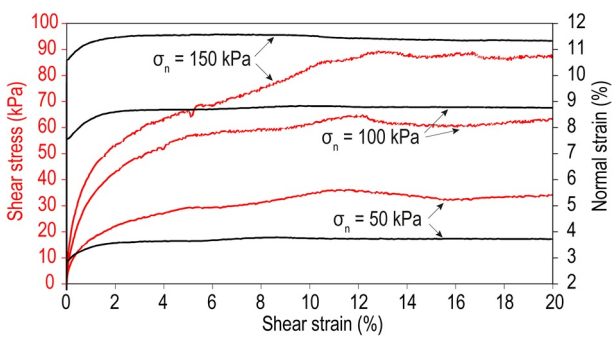

Figure 5. Shear stress-strain and normal strain curves for monotonic direct shear tests undertaken at normal effective stresses on disaggregated grains of rock (Tests 8, 9, and 10).

4.2.3. Monotonic Tests at σ_n = 150 kPa

Intact samples tested at a normal stress of 150 kPa displayed the highest peak (319.1 and 334.1 kPa) and residual shear stress (226.1 and 270.5 kPa) values observed in our baseline monotonic tests (Figure 3e). These samples displayed greater ductility than tests undertaken at lower normal stress values, though brittle stress drops (~35–70 kPa) were present in the post-peak phase. Sample dilation occurred following exceedance of peak shear stress, though to a lesser extent (normal strains of −0.54% to −2.64%; Figure 3f) than observed in samples tested at lower normal stresses.

Samples displayed a largely planar shear surface, with largely coherent upper and lower blocks (Figure 4c). Both samples displayed evidence of low angle cracking around the developing shear plane. In test 7, the

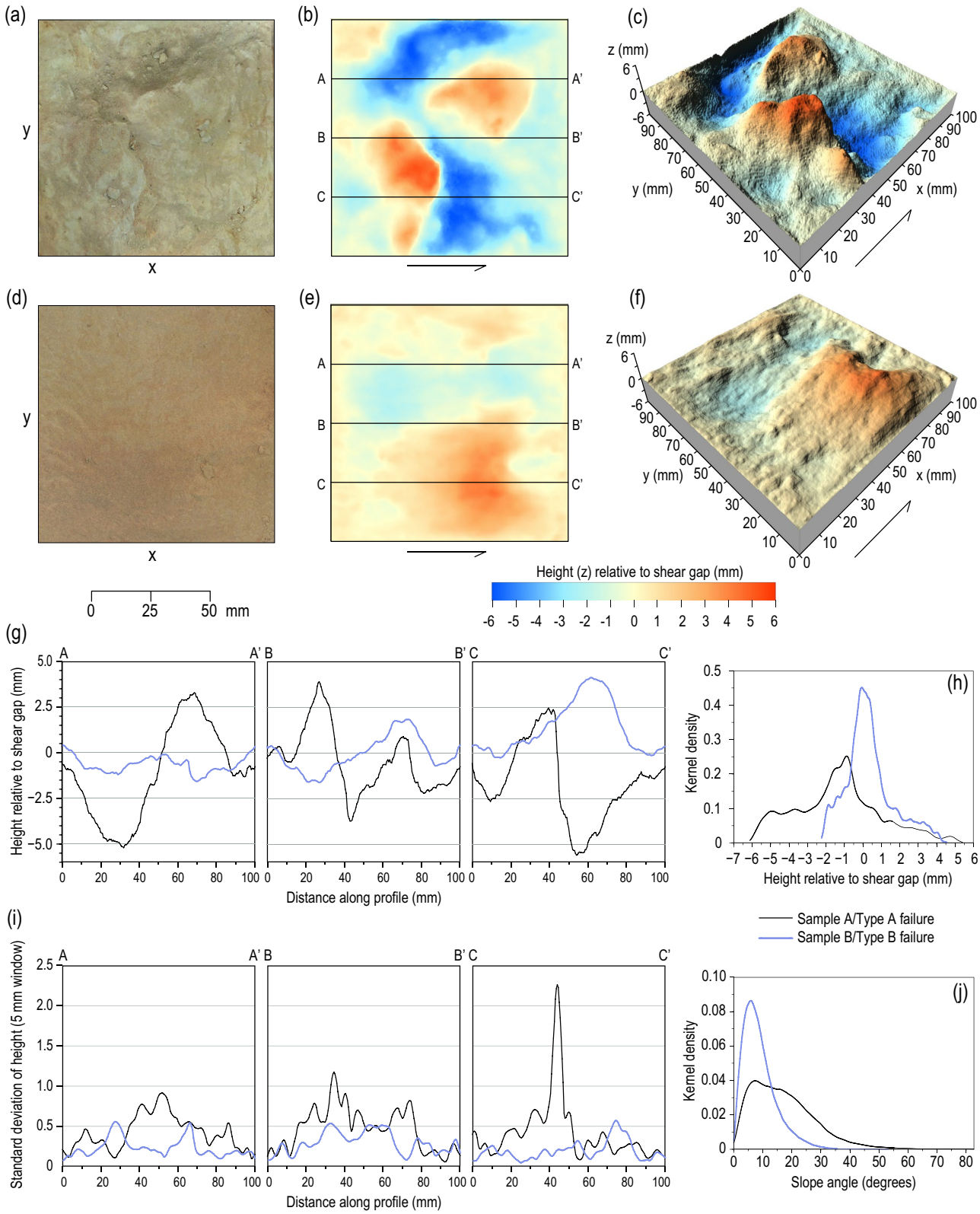
(a)
(b)
(c)
(d)
(e)
(f)
(g)
(h)
(i)
(j)
A
A'
B
B'
C
C'
x
y
z (mm)
x (mm)
y (mm)
0 25 50 mm
Height (z) relative to shear gap (mm)
-6 -5 -4 -3 -2 -1 0 1 2 3 4 5 6
Height relative to shear gap (mm)
Distance along profile (mm)
Kernel density
Sample A/Type A failure
Sample B/Type B failure
Standard deviation of height (5 mm window)
Slope angle (degrees)

Figure 6.

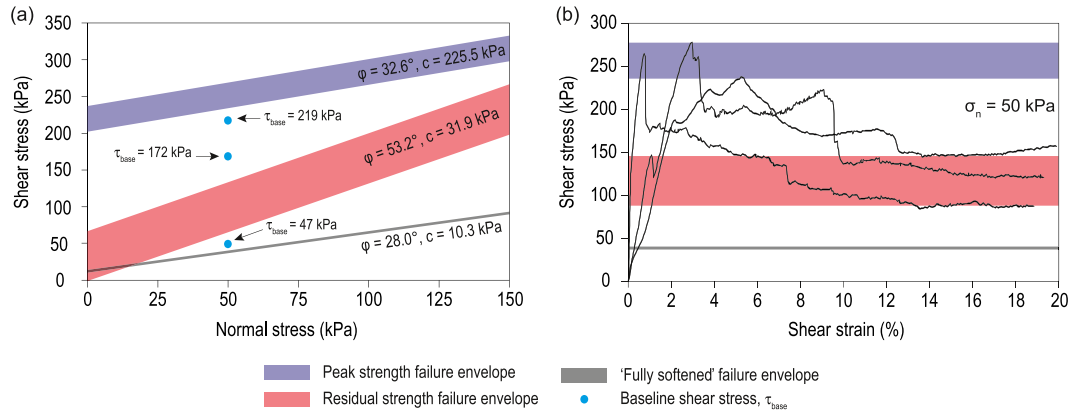

Figure 7. (a) Peak, residual and fully softened failure envelopes (best estimate ± one standard error) based on monotonic direct shear tests on Tubul Sandstone. Blue circles indicate baseline shear stress states used in dynamic tests. (b) Reference peak and residual strength envelopes for monotonic shear behavior at σ_n = 50 kPa, alongside underpinning stress-strain curves for monotonic direct shear Tests 1, 2, and 3 (Table 1).

sample continued to weaken after shear strain exceeded ~8%; this sample displayed the lowest degree of dilation and the most planar shear surface.

4.2.4. Monotonic Tests on Disaggregated Samples

Stress-strain curves for disaggregated samples (Figure 5) indicate a ductile rheology. During shearing, shear stress increased to peak values of 36.1 kPa (σ_n = 50 kPa), 64.9 kPa (σ_n = 100 kPa), and 89.4 kPa (σ_n = 150 kPa) and remained largely constant, with no reduction to a lower residual strength evident. During shearing, all three samples compressed by ~1% normal strain before reaching near-constant volume at shear strains greater than ~2%. All three disaggregated rock samples displayed a well-defined and fully planar shear surface; all shear deformation was directly accommodated along the shear gap.

4.2.5. Shear Surface Characterization

The SfM-derived DEMs and microtopographic data in Figure 6 permitted quantitative comparison of two characteristic failure surfaces and component asperities in samples tested in monotonic direct shear at normal stress values of 50 and 150 kPa immediately following exceedance of peak shear stress in each sample. These failure types represent the "end members" of the observed change from brittle-ductile to largely ductile behavior in response to increasing normal stress. Based on the patterns evident, we classified two types of failure surface. Samples tested at a normal stress of 50 kPa displayed a "Type A" failure surface, characterized by high-angle fractures (modal range of ~10–20°, with angles reaching 60°; Figure 6j) that extended both above (maximum of ~4.5 mm) and below (minimum of ~6 mm) the shear gap (Figures 6b, 6c, 6g and 6h). Type A failure surfaces are characteristically rough, as indicated by the standard deviation of heights over 5 mm sampling windows (Figure 6i; greater standard deviations indicate more variable topography). In contrast, samples tested at a normal stress 150 kPa displayed "Type B" failure surface. This type of failure is typified by a microtopography with a lower modal slope angle (~7.5°; Figure 6j) and a less rough shear surface (Figures 6e, 6f and 6i). Critically, Type B failures are more concentrated at the shear gap, with limited extension of asperities into the lower part of the sample (minimum of ~2.5 mm below the shear gap (Figures 6g and 6h).

Figure 6. Results of quantitative shear surface characterization using Structure-from-Motion (SfM) photogrammetry. The top-down orthophoto (a) and top-down (b) and obliquely viewed (c) digital elevation model (DEM) for Sample A (σ_n = 50 kPa, monotonic direct shear) are shown in the top row. The top-down orthophoto (d) and top-down (e) and obliquely viewed (f) DEM for Sample B (σ_n = 150 kPa, monotonic direct shear) are shown in the second row. For these images, heights are expressed relative to the shear gap (cf., Figure 2). In (b), (c), (e), and (f), the direction of travel of the lower section of the sample is indicated. The third row (g) and (h) allows comparison of the height profiles A–A', B–B', and C–C', shown in (b) and (e) taken parallel to the direction of shear in Samples A and B. Kernel density distributions of heights for both samples are displayed in (h). The standard deviation of height along profiles across the profiles (5 mm sampling windows) in each sample is displayed in (i). (j) Displays the kernel density distribution of topographic slope across the sample.

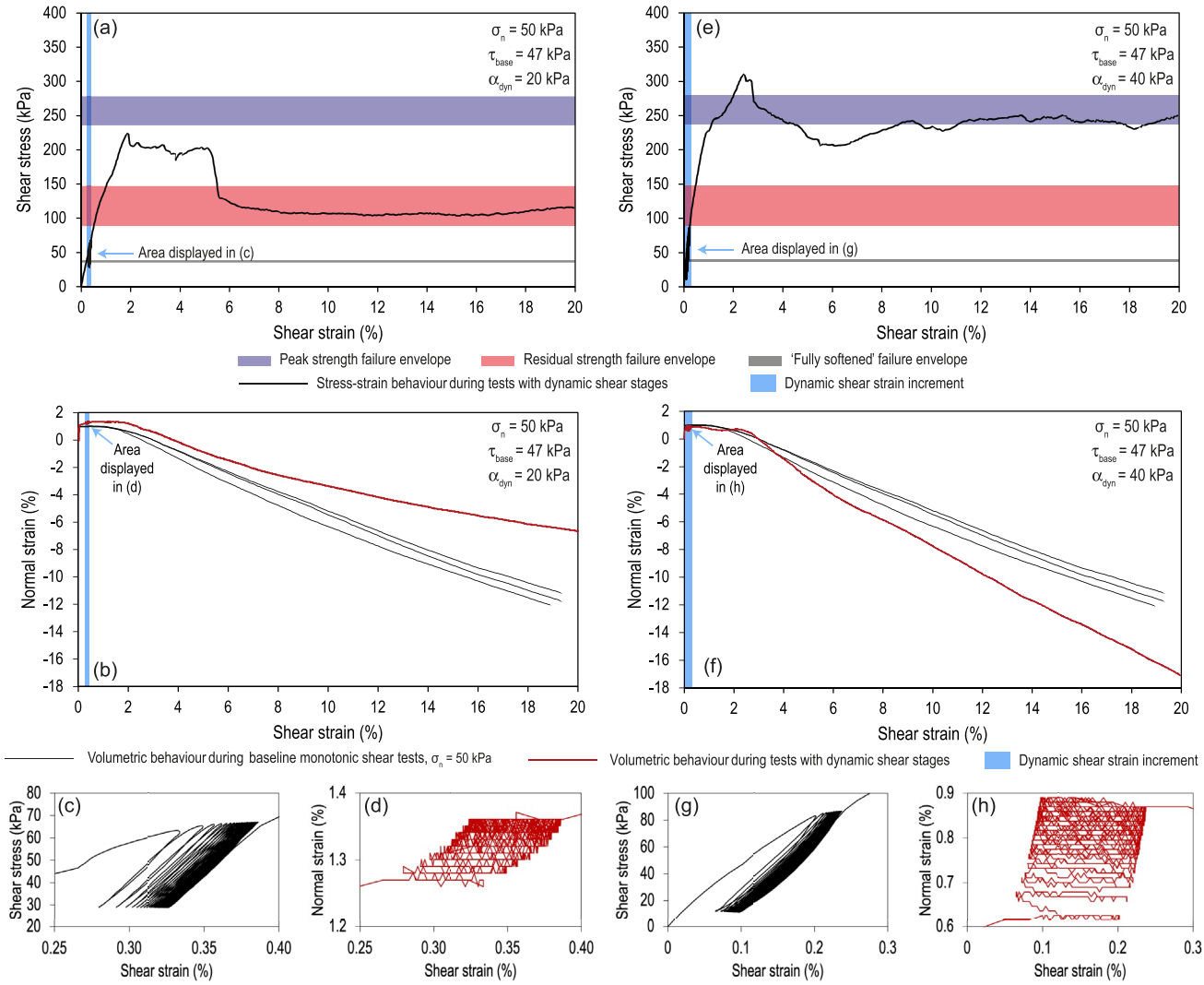

Figure 8. Shear stress-strain (a, c, e, and g) and normal strain (b, f, d, and h) behavior of intact rock samples subjected to dynamic direct shear at a normal stress of 50 kPa and a baseline shear reference shear stress value of 47 kPa. (a–d) show the results of Test 11 (dynamic shear stress amplitude of ±20 kPa). (e–h) show the results of Test 12 (dynamic shear stress amplitude of ±40 kPa). (c), (d), (g), and (h) display the sample behavior during dynamic loading stages.

4.2.6. Failure Envelopes

Peak, residual and fully softened failure envelopes are displayed in Figure 7a. The peak failure envelope for intact rock displayed a cohesion value, c, of 225.5 kPa and a friction angle, φ, of 32.6°. The residual strength failure envelope was defined by a lower cohesion (31.9 kPa) but a greater friction angle (53.2°). The fully softened failure envelope obtained from the disaggregated rock samples test data had the lowest observed cohesion (10.3 kPa) and friction angle (28.0°) in our baseline data set. These results reflect the gradual loss of cohesion and mobilization of frictional strength.

The reference peak and residual strength envelopes for monotonic shear behavior at a normal stress of 50 kPa (based on the minimum and maximum shear stress values observed; Section 3.3.2) are displayed alongside the underpinning stress-strain curves in Figure 7b.

4.3. Dynamic Direct Shear Behavior

4.3.1. Reference Dynamic Shear Stress Values, τ_{base}

Using the approach and rationale described in Section 3.3.3, our reference shear stress values during dynamic loading (τ_{base}) (σ_n = 50 kPa) were 47, 172, and 219 kPa (Figure 7a), indicative of increasing damage with the sample resulting from aseismic (gravitational) shear stress and associated strain accumulation.

4.3.2. Dynamic Tests, τ_{base} = 47 kPa

Stress-strain curves for dynamic shear tests at a reference shear stress (τ_{base}) of 47 kPa are displayed in Figure 8. During the low amplitude (α_{dyn} = 20 kPa) dynamic loading stage (test 11), the sample exhibited a total dynamic shear strain increment of ~0.08% (Figure 8c) and a total normal strain increment of ~0.1% (Figure 8d), indicating a reduction in sample volume (i.e., dynamic compaction). Following application of the low amplitude dynamic shear stress (α_{dyn} = 20 kPa), the sample initially contracted as shear proceeded (Figure 8b) and until peak shear stress (225.5 kPa) was achieved (Figure 8a). Notably, the sample was initially weaker than observed in baseline tests; peak shear stress values observed in baseline tests were not achieved. As shear proceeded, shear stress remained at ~200 kPa until ~5% normal strain, at which a brittle stress drop occurred and the sample reached a residual strength (~110–120 kPa) that was within the range observed in baseline tests, though this was achieved at a lower shear strain of ~5.5% (compared to ~10%–12% shear strain in the baseline data set). During post-peak monotonic shear, the sample began to dilate but to a lesser extent than observed in baseline tests (maximum normal strain of ~−6%). On inspection following completion, the surface was indicative of a degraded ("smoothed") Type B failure. Failure was concentrated along the shear gap, characterized by smoother, low angle asperities filled with disaggregated grains (Figure 4d).

During the high amplitude (α_{dyn} = 40 kPa) dynamic loading stage (test 12), the sample exhibited a total dynamic shear strain increment of ~0.08% (Figure 8g) and a total normal strain increment of ~0.28%, indicative of sample compaction (Figure 8h). Following application of the high amplitude dynamic shear stress (α_{dyn} = 40 kPa), peak shear stress increased to a peak of 311.2 kPa (Figure 8e); this value is ~30 kPa higher than the maximum shear stress observed in baseline tests. Following a post-peak and non-brittle reduction to a shear stress of ~205 kPa by ~6% shear strain, shear stress again increased to values equivalent to those of the peak shear stress seen in baseline tests. The sample did not show a reduction in shear strength; shear stress (~245 kPa) remained within the baseline peak shear strength envelope. The increase in sample shear strength in this sample was coincident with ongoing dilation throughout post-dynamic monotonic shear and exceeding that observed in the baseline shear tests (maximum normal strain of ~−17%) (Figure 8f). The failure surface of the sample was akin to a Type A failure; the highly dilated post-test sample displayed high angle fractures that extended throughout the height of the sample. We did not observe accommodation of enforced shear along the shear gap.

4.3.3. Dynamic Tests, τ_{base} = 172 kPa

Stress-strain curves for dynamic shear tests at a reference shear stress (τ_{base}) of 172 kPa are displayed in Figure 9. During the low amplitude (α_{dyn} = 20 kPa) dynamic loading stage (test 13), the sample exhibited a very minor total dynamic shear strain increment of ~0.02% (Figure 9c) and, similarly, a very small total normal strain increment of ~0.02% (Figure 9d). Following application of the lower-amplitude dynamic shear stress (α_{dyn} = 20 kPa), the sample displayed contractive behavior (Figure 9b) until peak shear stress (301.5 kPa) was achieved (Figure 9a). This was ~20 kPa greater than the maximum values observed in our baseline tests at a shear strain of 2%–3%, after which the sample weakened to a residual strength (~80–90 kPa) via a series of gradual and brittle stress drops. Transition to a residual strength comparable with, though ultimately ~20 kPa lower than, baseline tests was complete by a shear strain of 5.5%, after which the sample displayed ongoing dilation (~−6% normal strain at the end of the test) that was less pronounced than in baseline tests (Figure 10b). Following completion of the test, the shear surface displayed a highly degraded Type A failure surface characterized by a number of higher-angle fractures extending to the top and base of the sample, though these did not all accommodate shear deformation (Figure 4e). Instead, a well-defined, highly comminuted shear band was evident at the shear gap, separating the upper and lower blocks.

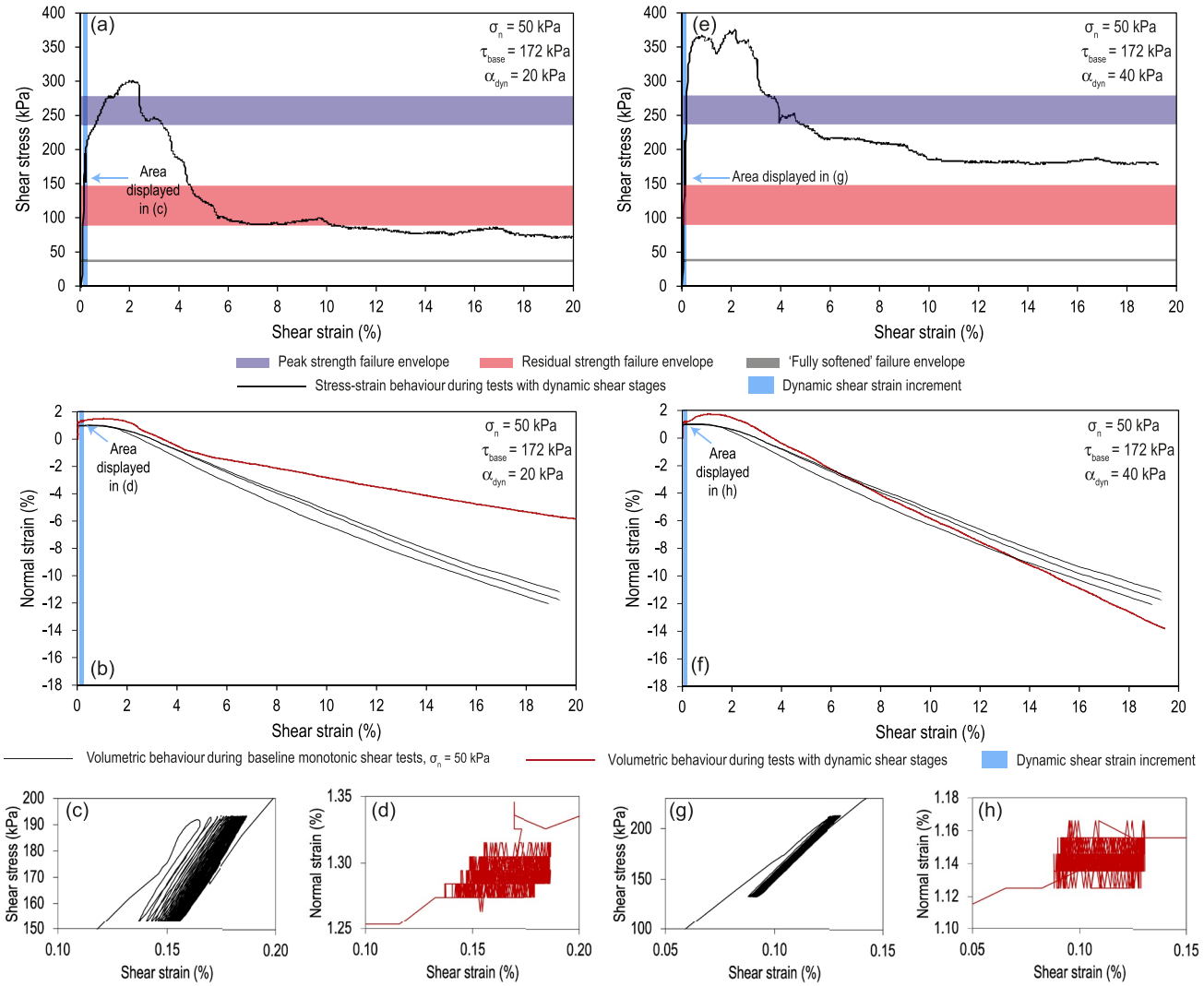

Figure 9. Shear stress-strain (a, c, e, and g) and normal strain (b, f, d, and h) behavior of intact rock samples subjected to dynamic direct shear at a normal stress of 50 kPa and a baseline shear reference shear stress value of 172 kPa. (a–d) show the results of Test 13 (dynamic shear stress amplitude of ±20 kPa). (e–h) show the results of Test 14 (dynamic shear stress amplitude of ±40 kPa). (c), (d), (g), and (h) display the sample behavior during dynamic loading stages.

During the high amplitude (α_{dyn} = 40 kPa) dynamic loading stage (test 14), the sample exhibited a total dynamic shear strain increment of ~0.01% (Figure 9g) and a total normal strain increment of ~0.01% (Figure 9h); strain accumulation during dynamic loading was negligible. Following dynamic shearing (α_{dyn} = 40 kPa), the sample displayed an increase to a peak shear stress of 377.4 kPa (Figure 9e) — a value ~100 kPa greater than observed in baseline tests — and a slight reduction in sample volume (Figure 9f). Increased shear strength persisted until a brittle stress drop occurred at ~3% shear strain; shear strength then reduced to a residual condition (~180 kPa), though this remained greater than that observed in baseline tests. The sample also dilated more (~−14% normal strain at the end of the test) than was observed in baseline tests. The post-failure sample displayed several high angle and sheared asperities extending throughout the height of the sample, and a gouge-filled shear band along the shear gap (Figure 4f).

4.3.4. Dynamic Tests, τ_{base} = 219 kPa

Stress-strain curves for dynamic shear tests at τ_{base} = 219 kPa and where α_{dyn} = 20 kPa are displayed in Figure 10. During the low amplitude (α_{dyn} = 20 kPa) dynamic loading stage (test 15), the sample exhibited a total dynamic shear strain increment of ~0.1% (Figure 10c) and did not accumulate detectable normal strain

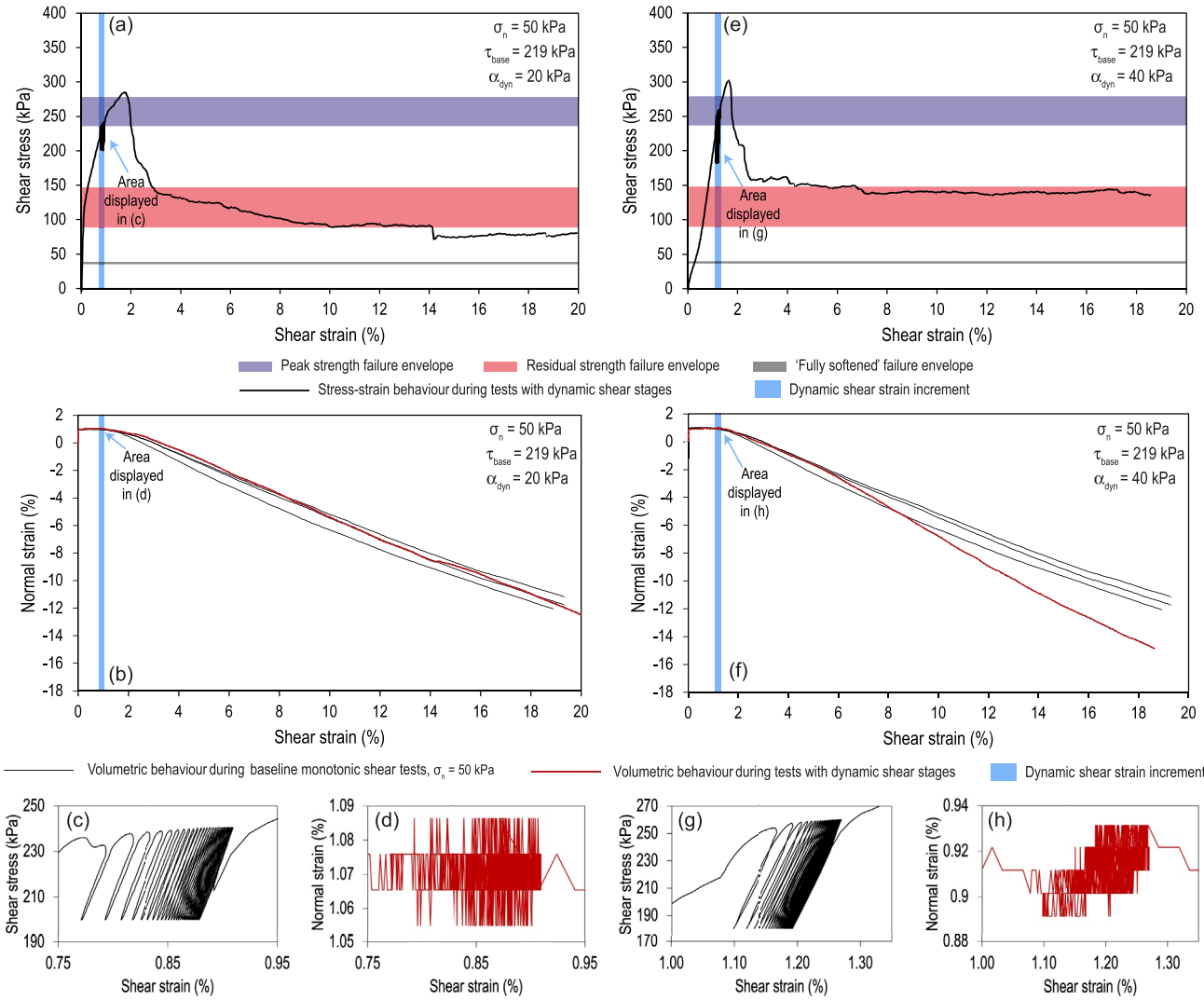

Figure 10. Shear stress-strain (a, c, e, and g) and normal strain (b, f, d, and h) behavior of intact rock samples subjected to dynamic direct shear at a normal stress of 50 kPa and a baseline shear reference shear stress value of 219 kPa. (a–d) show the results of Test 15 (dynamic shear stress amplitude of ±20 kPa). (e–h) show the results of Test 16 (dynamic shear stress amplitude of ±40 kPa). (c), (d), (g), and (h) display the sample behavior during dynamic loading stages.

(Figure 10d). In subsequent monotonic shear, the sample displayed peak shear strength (285.6 kPa) that was very marginally (<10 kPa) greater than the maximum observed in baseline tests, before undergoing brittle failure to shear stress values within the baseline range of residual strength at ~3% shear strain (Figure 10a). However, shear stress continued to decrease until 10% shear strain, before stabilizing at ~90 kPa and then undergoing a brittle stress drop at 14% shear strain that lowered shear stress to values below those observed in baseline tests ($\tau \approx 75$ kPa). Throughout the test, the volumetric behavior was dilatant, and largely within the range observed in baseline tests (Figure 10b). After the test, the sample was heavily fractured and dilated, with multiple sub-vertical cracks extending from the shear plane to the top and base of the sample and evidence of a highly comminuted shear band along the shear gap.

During the high amplitude ($\alpha_{dyn} = 40$ kPa) dynamic loading stage (test 16), the sample exhibited a total dynamic shear strain increment of ~0.15% (Figure 10g) and a total normal strain of ~0.03% (Figure 10h). This dynamic shearing ($\alpha_{dyn} = 40$ kPa) was followed by an increase to a peak shear stress of 303.0 kPa (Figure 10e), which is ~25 kPa higher than the maximum observed in baseline tests. The sample underwent two brittle stress drops between shear strain values of 2% and 3%, before reaching a residual strength (~140 kPa) within the range observed in baseline tests. The sample also displayed dilative behavior similar to that ob-

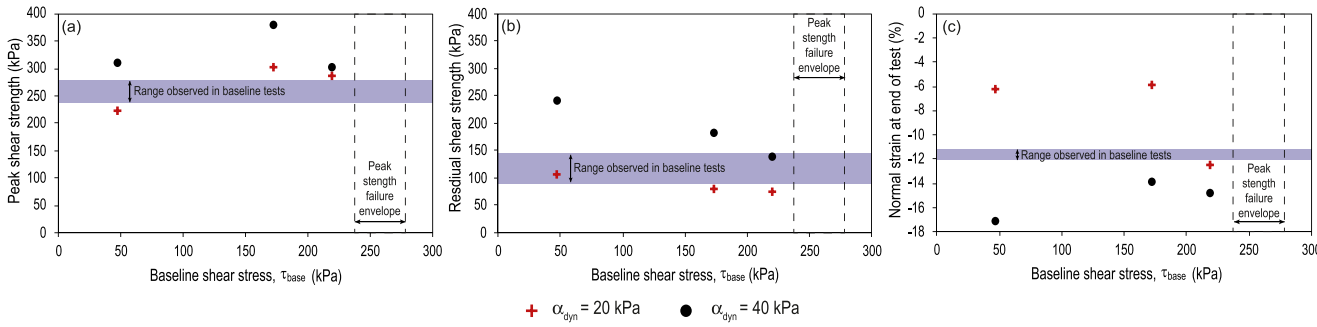

Figure 11. Summary of the effects dynamic shear loading on key metrics of shear behavior plotted against baseline shear stress values. (a) Post-dynamic peak shear strength. (b) Post-dynamic residual shear strength. (c) Normal strain values at the end of each test (~18%–20% shear strain). The dynamic shear stress amplitude in each test is indicated by the symbol used. For each metric, the range of values observed in baseline tests is displayed in each plot.

served in baseline tests until ~6% shear strain, when the rate of dilation relative to shear strain increased, coincident with a final drop in shear stress to near-constant residual strength (Figure 10f). The post-test sample was heavily fractured and dilated, with a well-developed shear band.

4.3.5. Overview of Test Results

During the dynamic stages of all tests, all samples tested displayed evidence of shear-strain hardening. The highest total dynamic shear strain increments were observed in tests 15 and 16 (τ_{base} = 219 kPa). The highest normal strain increments occurred in tests 11 and 12 (τ_{base} = 47 kPa), indicating the greatest amount of sample compaction during dynamic loading. In tests 13 to 16 inclusive (τ_{base} = 172 kPa; τ_{base} = 219 kPa), volume changes recorded during dynamic loading were an order of magnitude smaller and/or not detectable within the resolution of the DynBPS. Tests 13 and 14 (τ_{base} = 172 kPa) exhibited relatively very minor shear and normal strain accumulation during dynamic shear.

To allow simpler comparison between the results of each test during post-dynamic monotonic shear, Figure 11 summarizes the relationships between the baseline shear stress (47, 172, or 219 kPa) used in dynamic tests and three key metrics that summarize the strength and rheology of samples in response to low amplitude (α_{dyn} = 20 kPa) and high amplitude (α_{dyn} = 40 kPa) dynamic loading: peak shear strength (kPa) (Figure 11a), residual shear strength (mean shear stress for shear strain values between 15% and 18% in monotonic tests, as outlined in Section 3.3.2; Figure 11b) and normal strain observed at the end of test (%).

Samples subjected to high-amplitude dynamic loading displayed peak and residual shear strength values that are consistently greater than those subjected to low-amplitude dynamic loading, and greater than the range observed in baseline tests (Figures 11a and 11b). However, at greater baseline shear stresses, the effect of dynamic shear stress amplitude on peak shear strength diminished, as evidenced by smaller differences in peak shear strength values between (a) tests subjected to different dynamic loading amplitude; and (b) the peak shear strength values recorded in dynamic tests and those from baseline monotonic tests. The residual strength of samples subjected to low-amplitude dynamic loading was within, or very close to, the range observed in baseline tests (Figure 11b). In contrast, the residual strength of samples subjected to high-amplitude dynamic loading decreased as the baseline shear stress increased, and was ultimately within the range observed in baseline tests where τ_{base} = 219 kPa.

All samples subjected to high-amplitude dynamic loading displayed a greater degree of dilation (negative normal strain values) than was observed in baseline monotonic tests (Figure 11c). In contrast, samples subjected to low-amplitude dynamic loading displayed either a lower degree of dilation relative to that observed in baseline monotonic tests (τ_{base} = 47 kPa and τ_{base} = 172 kPa), or normal strain that was very close to that observed in baseline test (τ_{base} = 219 kPa) (Figure 11c).

In all dynamic tests, we also note key qualitative differences in post-dynamic sample behavior relative to baseline monotonic shear tests. We observed that the shear strain at which transition from peak to residual strength is largely complete (i.e., the vast majority of strength loss had occurred following, for example, a brittle stress drop) was generally considerably (>50%) lower than the range observed in baseline monotonic

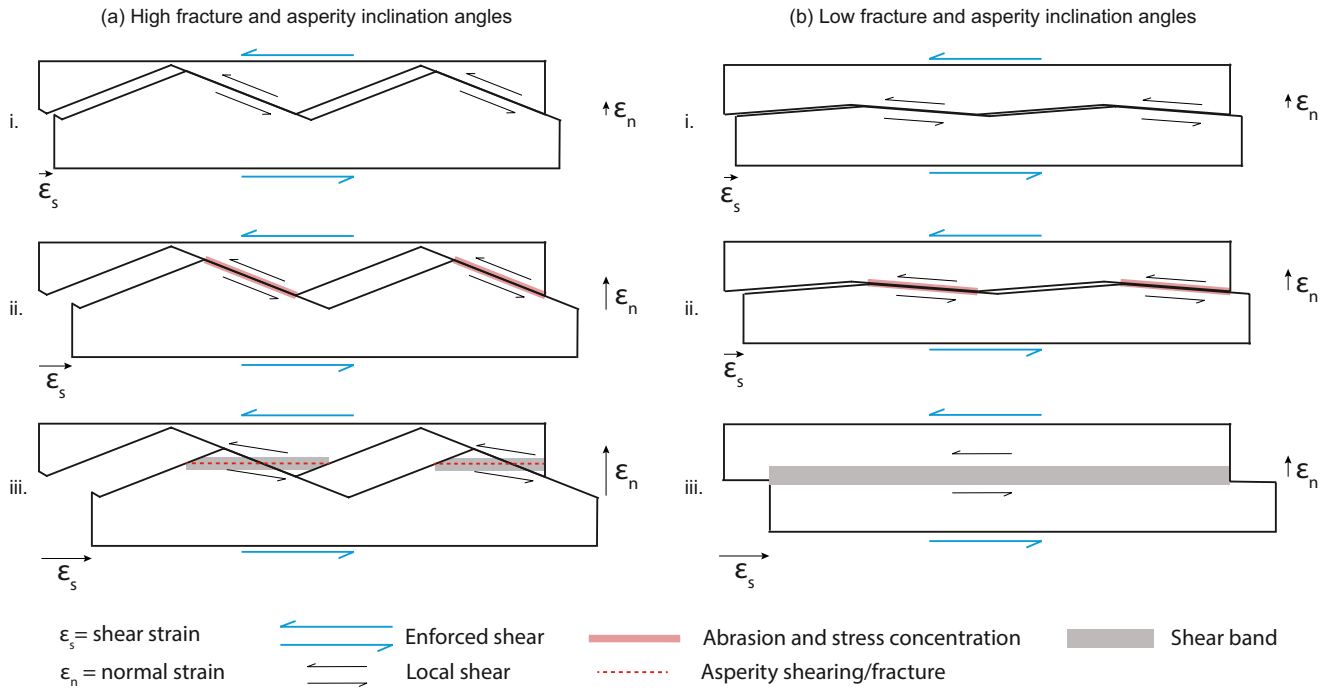

Figure 12. Conceptual summary of the control of fracture and asperity angle on failure mechanism and dilation. In (a), high fracture angles result in shear deformation being accommodated along asperities (a i), causing abrasion and stress concentration along shear pales and within asperities (a ii). As dilation proceeds, stress concentration results in shearing through asperities, causing the formation of a shear band along the shear gap (a iii). Subsequent shear is accommodated both along this shear band and along asperities. In (b), shear along low fracture asperities requires less dilation (b i). Subsequent frictional sliding, abrasion and comminution as shear proceeds (b ii) cause the formation of a more discrete shear band focused along the shear gap (b iii).

tests; dynamic loading resulted in transition to a post-peak, residual strength being achieved at a lower shear strain.

5. Discussion

5.1. Deformation Mechanisms in Baseline Monotonic Shear Tests

The differences in shear strength and rheology observed between baseline monotonic direct shear tests undertaken at different normal stresses can be explained in terms of the nature and evolution of the shear surface that formed. Baseline monotonic tests where σ_n = 50 kPa displayed consistently highly dilatant behavior resulting from the formation of high-angle asperities (shear surface irregularities) that formed as shear proceeded (Ladanyi & Archambault, 1969; Lajtai, 1969a, 1969b; Patton, 1966; Pereira & de Freitas, 1993). Higher asperity angles can increase net shear strength by causing a greater degree of interlocking between discontinuity surfaces (Barton, 1973, 1976; Barton & Choubey, 1977; Jaeger, 1971; Patton, 1966). In our baseline monotonic tests (σ_n = 50 kPa), shear was accommodated as frictional sliding along higher angle planes oblique to the direction of enforced shear, resulting in the observed sample dilation (e.g., Lajtai, 1969a; Selby, 1993; Wyllie, 1999) (Figure 12a). As shear deformation and dilation proceeded, voids were created within the rock as the upper discontinuity surface moved away from the lower surface (Pereira & de Freitas, 1993) (Figure 12a). Contact areas along sliding surfaces reduced such that stresses concentrated on and within asperities, ultimately exceeding local strength and causing abrasion, crushing, and shearing through the asperities (Bahaaddini et al., 2016; Fathi et al., 2016; Hutson & Dowding, 1990; Pereira & de Freitas, 1993; Wyllie, 1999). Shearing through asperities is evident in the stress-strain curves as brittle stress drops (Figure 3a). Subsequently, a lower-strength, less rough band of comminuted rock formed as shearing primarily concentrated along the shear gap as internal friction was mobilized, rather than frictional sliding along oblique tension cracks (Figure 12a). The more gradual strength reductions observed were indicative of frictional and dilative sliding, stress redistribution, and abrasion along remaining asperities.

In monotonic tests at greater normal stresses, the presence and effect of high-angle fractures became less significant (Figure 12b). Whilst oblique tension cracks were evident in samples tested at normal stresses of 100 and 150 kPa (Figures 4a and 4b), shear was increasingly accommodated along the shear gap. As normal stress increased, the growth of tensile cracks and resultant asperities was suppressed; under increasing normal stress, tensile stresses propagated into asperities rather into the surrounding intact rock (Bahaaddini et al., 2016). As such, incipient asperities were crushed and sheared off to form a discrete shear band more closely aligned with the direction of enforced shear, and before oblique tension cracks could be mobilized to accommodate shear deformation with accompanying sample dilation (Figure 12b). Resultantly, fewer brittle stress drops and reduced dilation were observed in our monotonic tests at normal stresses of 100 and 150 kPa. Post-peak strength resulted from friction within the comminuted shear band. The shear strength of fully disaggregated rock (Tests 8, 9, and 10; Table 1) was considerably (100–200 kPa) lower than the residual strength of "intact" samples at equivalent normal stress values. This suggests that none of the monotonic tests on intact samples was fully comminuted and softened by ~20% shear strain, and so considerable further shear strain must accumulate before the fully softened strength condition is achieved. Hence, ongoing crushing and abrasion of the rock may explain the reduction in, but not total absence of, cohesion in the residual and fully softened strength envelopes (Figure 7a).

The largest reductions in strength between peak and residual conditions were observed in monotonic tests where $\sigma_n = 50$ kPa, reflecting a change in the location of mobilized friction, from high-angle asperities to degraded asperities and generated gouge. Such post-peak reductions in strength were less pronounced at higher normal stresses (Figure 3). A greater degree of post-peak frictional strength was maintained in tests where $\sigma_n = 100$ kPa and $\sigma_n = 150$ kPa; frictional sliding along the shear gap remained the dominant shearing mechanism in both the peak and residual phases. These differences in shearing mechanism as normal stress increased explain the steeper residual strength failure envelope and, hence, friction angle relative to the peak strength failure envelope (Figure 7a). The importance of normal stress and, hence, depth of the shear surface in controlling the inception of oblique tension cracks suggests that shallower landslides are more prone to changes in shear behavior in response to seismic loading, justifying both our focus on the effects of dynamic loading where $\sigma_n = 50$ kPa, and supporting broader field and laboratory observations (e.g., Sepúlveda et al., 2016).

5.2. Deformation Mechanisms in Dynamic Shear Tests

Despite intrinsic variability in the range of key metrics describing shear behavior observed in the baseline monotonic data set, we noted consistent differences, patterns and trends in behavior in dynamic shear tests, indicative of fundamental differences in underpinning, causative shear mechanisms (Figure 11). Direct observations of the nature of the shear surface and data describing the magnitude of normal strain provide strong evidence to mechanistically explain the observed differences in behavior (Figures 4, 6 and 11). In combination, our data and observations indicate that the effects of dynamic loading on post-dynamic shear behavior extend beyond wide and inherent sample variability. Based on our data, observations and comparisons with the baseline monotonic data set, we interpret and explain the variability in shear behavior as follows, noting that differences in strength and behavior relate directly to specific deformation processes.

The low amplitude (±20 kPa) dynamic loading at a reference shear stress (τ_{base}) of 47 kPa resulted in a reduction in peak shear strength relative to our baseline monotonic data set (Figures 8a and 11). We contend that the lower amplitude shear stress was insufficient to initiate or propagate oblique tension cracks throughout the sample, and crack damage and abrasion were concentrated along the shear gap (Figure 4d), potentially assisted or facilitated by the increased compaction experienced during dynamic loading, predisposing this area to quasi planar failure during subsequent monotonic shear (Figure 12b iii). Any high angle fractures that formed during and/or following dynamic loading were not fully mobilized to accommodate enforced shear, and so the sample experienced reduced dilation relative to that observed in baseline tests (Figure 11c). Abrasion, comminution, and shearing through asperities within the shear band is evident in the stress-strain curve (Figure 8a) as the zone of near-constant shear stress following peak shear strength and until ~5% shear strain, until brittle failure of remaining asperities occurred and the sample strength reduced to a residual condition. In contrast, high amplitude (±40 kPa) dynamic loading was sufficient to cause initiation of high angle tension cracks (Cai et al., 2004; Eberhardt et al., 1999) that rapidly propa-

gated, facilitated by a lower fracture toughness at a greater cyclic strain rate (e.g., Erarslan, 2016; Hernández-Gómez et al., 2004). Following dynamic loading, the upper and lower blocks initially interlocked to cause slight compaction of the sample before fracturing of remaining rock bridges at peak shear strength. Enforced shear was accommodated by shearing along these high angle fractures, causing enhanced sample dilation (Figure 11c) that continued until 20% shear strain (Figure 8d). As shear strain accumulated, the strength of thicker and so more resistant asperities was not exceeded (Yin et al., 2020); degradation or brittle shearing through high-angle asperities and a reduction to the residual strength condition observed in baseline tests did not occur. As such, there was no reduction to a conventional lower, "true" residual strength condition (Figures 8c and 11c).

At a baseline shear stress (τ_{base}) of 172 kPa, the degree of pre-dynamic damage and accumulated shear strain had increased; a set of incipient tension fractures had formed before the samples were subjected to dynamic loading. This resulted in variations in behavior as incipient fractures and asperities were variably exploited by dynamic loads of different amplitude. The low amplitude (±20 kPa) dynamic loading caused incipient fractures to extend (Figure 4e), and dynamic loading resulted in abrasion and damage to asperities in a mid-sample shear band. During post-dynamic monotonic shear, the shear deformation along enhanced tension cracks was initially mobilized, evident as an elevated peak shear stress and initial sample compaction followed by dilation. However, as favorably aligned asperities weakened during dynamic loading were abraded and/or sheared off, evident as stress drops in the stress-strain curve (Figure 9a), shear deformation was then accommodated at the shear band and less sample dilation was required (Figure 9b) as the shear strength reduced to, and ultimately fell below, the baseline residual strength condition. This suggests that low amplitude dynamic loading caused a greater degree of strength degradation along and within existing asperities; once this had occurred, asperity degradation occurred over a smaller shear strain increment than in baseline tests and continued to occur throughout the test. In contrast, tension cracks that rapidly propagated during high amplitude (±40 kPa) dynamic loading were initially mobilized, causing contraction of the sample and a greater peak shear stress relative to baseline monotonic tests (Figure 11a). Shearing through asperities that formed during pre-dynamic shear resulted in a stress drop to a persistent lower strength condition, but this was greater than the residual strength observed in baseline tests (Figure 11b). The greater post-dynamic dilation observed in this dynamic test (Figure 11c) suggests that enforced shear was accommodated along high angle fractures to a greater extent (Figure 4f), rather than along a weaker, comminuted shear band.

At a baseline shear stress (τ_{base}) of 219 kPa, differences in peak and residual shear strength from those observed baseline tests were less pronounced because the formation of fractures and asperities typical of baseline conditions had already occurred; these were not significantly altered by subsequent dynamic loading and typical baseline shear behavior was only marginally modified, if at all (Figures 11a and 11b). We noted slightly elevated peak shear strength values following dynamic loading. We again consider this to be indicative of enhanced tensile cracking during dynamic loading and short-lived accommodation of enforced shear along resultant asperities before deformation was focused along the pre-weakened ("monotonic") shear band. We also observed a reduction in shear strength to residual values at a considerably lower shear strain than in baseline tests; prolonged post-peak strength resulting from ongoing asperity degradation observed in baseline tests was not evident in these dynamic tests, likely resulting from, relative to baseline conditions, premature asperity degradation during dynamic loading (Belem et al., 2007; Ferrero et al., 2010), consistent with greater dynamic shear strain accumulation.

5.3. Path Dependence of Post-Seismic Hillslope Behavior

Our results illustrate the fundamental importance of two key factors in generating differences in the character of fractures and asperities within rocks: (a) the amplitude of the dynamic load applied to the sample; and (b) the degree of accumulated shear strain prior to the commencement of dynamic loading. These differences control the relative importance and contribution of key deformation mechanisms (dilative frictional sliding vs. asperity degradation) that are mobilized to accommodate subsequent monotonic shear, equivalent to post-seismic hillslope deformation. In turn, the relative contribution of these mechanisms can result in differences in strength and rheology, such that post-dynamic sample behavior and, by implication, post-seismic hillslope behavior is path dependent (e.g., Phillips, 2006; Temme et al., 2015), contingent on

the specific nature of ground shaking experienced previously. The path-dependent effects of dynamic stress history on strength and rheology were most pronounced in tests carried out at the lowest baseline shear stress (τ_{base} = 47 kPa), broadly equivalent to shallow ($z \leq 5$ m) landslides on hillslopes of 30°–40° that are most prone to failure during seismic events (Section 3.3.3). These hillslope configurations are characterized by limited damage and pre-existing shear surface development (Eberhardt et al., 1999; Petley et al., 2005). When subjected to low amplitude dynamic shear stresses, such hillslopes are weakened and hence are more likely to fail in the post-seismic phase in response to, for example, rainfall (Lin et al., 2008; Marc et al., 2019). In contrast, high amplitude dynamic shear stresses generate oblique tension cracks in hillslopes of this configuration, with a resultant increase in post-seismic strength and a less brittle rheology. As such, in this context, "damage" is too general and vague a term to describe the range of potential deformation mechanisms that can influence hillslope behavior; the specific nature of damage and how this influences the nature of shear-zone deformation is critical and, in turn, can influence post-seismic stability, and styles and rates of landslide deformation (Bjerrum, 1967; Clarke & Burbank, 2011; Gischig et al., 2015; Stead & Wolter, 2015). This variable response, and the strong legacy of past ground shaking via accumulated damage, likely contributes to the scatter observed in empirical and process-based numerical predictions of the number, area, volume and/or spatial distribution of landslides resulting from large earthquakes, in which the strength properties of hillslopes are not directly considered and/or are assumed constant (Jibson, 1993; Marc et al., 2016). Indeed, the significance of variability in hillslope strength, both spatially and temporally, on the predictive capacity of numerical models of coseismic landsliding has previously been acknowledged (Dreyfus et al., 2013). This is potentially particularly the case for hillslopes of this general hillslope configuration ($z \leq 5$ m; $\beta = 30°–40°$).

Our results indicate that susceptibility to path-dependent behavior in response to dynamic shear stress amplitude becomes less marked at greater baseline shear stresses and, hence, landslides with more developed shear surface. Our intermediate baseline shear stress condition (τ_{base} = 172 kPa), broadly equivalent to landslides where $z \approx 20–25$ m and $\beta \approx 35°–40°$, displayed relative strengthening relative to baseline shear conditions, but this was more pronounced following the high amplitude dynamic loading. In addition, post-peak strength remained greater than that observed in baseline monotonic shear following high amplitude dynamic loading. At greater baseline shear stresses (τ_{base} = 219 kPa; equivalent hillslope configuration: $z \approx 30–35$ m; $\beta \approx 35°–40°$), the strength characteristics were similar to those observed in baseline shear tests. Increasingly deep-seated landslides are therefore less prone to divergent post-seismic behavior resulting from differences in dynamic loading amplitude and, by implication, the magnitude of seismic ground accelerations. However, in these deeper landslide settings, dynamic loading can, via asperity degradation, decrease the shear strain by which full transition from peak to residual strain occurs. In our baseline monotonic tests, this process was complete by ~13%–14% shear strain, but was lower (~3%–6%) in dynamic tests; dynamic asperity degradation can increase the brittleness of rocks. In field settings where aseismic shear stress is less than peak strength but greater than residual strength of the rock mass, this effect will be manifest in slow and/or episodically moving landslides as reductions in the strain that a hillslope can sustain before failing in the post-seismic phase. We note this reduced strain at failure is not dependent on the amplitude of shear stress used in the dynamic test, and appears to be a more universal effect of dynamic loading. Whilst progressive or episodic strains may be more readily detectable using remotely sensed data in larger, deeper-seated landslides (e.g., Bekaert et al., 2020), this does not preclude their occurrence or significance in shallower landslides. For example, accelerating patterns of pre-failure creep have been observed in high spatial (10^{-3}–10^{2} m^3) and temporal (~hourly to monthly) resolution field-scale monitoring campaigns in brittle materials (Rosser et al., 2007; Royán et al., 2015). The lower resolution (~monthly to annual) datasets used to map co- and post-seismic landslides may not be of sufficient spatiotemporal resolution to capture progressive and/or episodic strain accumulation in smaller, shallower landslides (Cooper et al., 1998; Dietze, Mohadjer, et al., 2017; Dietze, Turowski, et al., 2017; Williams et al., 2019). Shallow landslides may therefore also deform episodically or continuously (via creep) in the post-seismic phase until a "critical strain" is achieved, at which point the hillslope becomes unstable if the hillslope-forming materials are prone to brittle-type failure and a reduction to residual strength conditions (Chandler & Skempton, 1974; Petley et al., 2005). On the basis of our experiments, this critical strain will be reduced relative to pre-seismic conditions following dynamic loading. It is therefore possible that brittle hillslopes experiencing greater reductions in tolerable (critical) strain will likely fail sooner in response to a combination of meteorological

and/or seismic forcing and/or autogenic creep deformation. The overall distribution and exploitation by forcing factors of this post-seismic tolerable strain within a landscape may, in turn, contribute to the temporal pattern of post-seismic landslide activity observed by Marc et al. (2015) in regional landslide inventories.

Our results, and the understanding of underpinning shear deformation mechanisms they provide, indicate that there is no single or pre-determined post-seismic landslide behavior trajectory following an earthquake. Our findings add broader context to previous observations and/or assumptions that ground cracking and damage resulting from coseismic ground shaking causes a reduction in hillslope strength, predisposing hillslopes to failure in the post-seismic phase (Marc et al., 2015; Parker et al., 2015). Instead, hillslope strength can be unaltered, increased (strengthened) or decreased (weakened) by seismic loading events of differing character, and so generalizing regional-scale rates and patterns of post-seismic landsliding in response to a single earthquake event is unlikely to be valid in, and transferable across, all seismic settings and at all scales (Kincey et al., 2021; cf., Marc et al., 2015). Rates and patterns of post-seismic landsliding are at least in part controlled by the nature of coseismic ground shaking at a specific location and how this influences the strength and rheology of slope-forming rocks. Our findings form part of a wider and growing body of work that demonstrates the importance of lithology, local- to regional-scale geomorphology, stress history and landslide mechanism in controlling post-seismic hillslope behavior and variability therein (Brain et al., 2017; Carey et al., 2021; Hu et al., 2018; Kincey et al., 2021). As such, invoking a range of poorly constrained, extrinsic and universal "healing" mechanisms to explain observed trajectories and temporal trends in the rate of new landslides may not be necessary or appropriate at all spatial scales. The post-seismic behavior of landslides is contextual, dependent in part on the type of landslide, the underlying mechanisms that govern strain accumulation and the broader intrinsic and extrinsic controls thereon (Bjerrum, 1967; Chen et al., 2020; Dahlquist & West, 2019; Kincey et al., 2021; Petley et al., 2005).

5.4. Broader Significance

The intact strength of the Tubul Sandstone is low ("very weak"); our findings are therefore most directly transferable to rock types of comparable density and strength (e.g., the sedimentary and metasedimentary rocks of Taiwan — see Lin et al., 2008). The estimated σ_{UCS} of the Tubul Sandstone is up to two to three orders of magnitude lower than many competent sedimentary, igneous and high-grade metamorphic rocks (e.g., Attewell & Farmer, 1976; Heap et al., 2009; Vinciguerra et al., 2005). It is therefore important to consider how transferable our findings and causative deformation mechanisms are to a broader range of lithologies of different strength and found in different physiographic and tectonic settings.

The design of our dynamic testing program was informed by critical cracking thresholds that have been observed to be consistent across different rock types, expressed relative to σ_{UCS} (Cai et al., 2004; Lou et al., 2019). In addition, the key controls on mechanisms of deformation, and so strength and rheology, of fractured rock have been observed to be widely applicable, with a firm theoretical basis and support from empirically validated numerical models (Bahaaddini et al., 2013; Belem et al., 2007; Ferrero et al., 2010; Jafari et al., 2004; Lajtai, 1969a, 1969b; Patton, 1966; Pereira & de Freitas, 1993). Consequently, it is reasonable to assume that our key findings about the importance of the amplitude of dynamic loading and the degree of shear surface formation in generating asperities of differing character are broadly transferable to a range of lithologies and hillslope settings (Lin et al., 2008). The critical interplay between in situ aseismic shear stresses, accumulated damage, cracking thresholds and the amplitude of seismic shear stresses is therefore unlikely to be limited to the Tubul Sandstone; path-dependent post-seismic shear behavior is likely to be critical in a range of lithologies and slope settings.

5.5. Spatial Distribution and Scale of Observed Effects

Since the intensity of ground shaking that drives differences in strength and rheology evident in our data set also varies across and between epicentral landscapes, we can reasonably expect hillslopes to display differing responses to an earthquake in the post-seismic phase, governed in part by the broader controls on the regional to local intensity of shaking. First-order controls on the occurrence of coseismic landslides are seismological and include fault mechanism, rupture depth and seismic moment (Keefer, 1984; Rodríguez et al., 1999). The specific spatial pattern and density of coseismic landsliding also critically depends on

regional seismic wave attenuation and, hence, ground shaking intensity with distance from the earthquake rupture surface (Meunier et al., 2007). This pattern is further modified by local slope factors, including slope angle (Jibson et al., 2000; Newmark, 1965), topographic amplification (Buech et al., 2010; Meunier et al., 2008; Sepúlveda et al., 2005) and local-slope modification of seismic wave properties and ground accelerations, including the amplitude and frequency content and duration of ground accelerations (Burjánek et al., 2012; Lenti & Martino, 2013; Moore et al., 2011). In locations where these regional to local factors are not conducive to ground accelerations sufficient to cause near instantaneous coseismic hillslope failure, the range of deformation mechanisms observed in our tests can be mobilized by sub-threshold accelerations and resultant dynamic shear stresses. In these locations, both the amplitude of dynamic shear stresses and the specific hillslope configuration (and so degree of aseismic shear surface development) can control the post-seismic behavior of hillslopes. Based on our initial estimations of equivalent horizontal ground accelerations that cause dynamic shear stress amplitudes of ±20 and ±40 kPa (Section 3.3.3), we note the potential existence of a threshold ground acceleration between ~0.33 and ~0.66 g that may be sufficient to cause divergent, path-dependent post-seismic landslide behavior in shallow landslides. Where both sufficiently dense seismometer networks and detailed landslide inventories are available, it may therefore be possible to identify local to regional differences in post-seismic hillslope stability in zones of varying coseismic ground accelerations for different hillslope configurations (Buech et al., 2010; Meunier et al., 2007; Rault et al., 2020).

5.6. Modeling Path Dependence of Post-Seismic Hillslope Behavior

The post-dynamic mechanisms of the observed path dependence of hillslope behavior have been modeled and validated at a range of scales, from laboratory and shear-surface settings (e.g., Belem et al., 2007) to jointed rock slope applications (e.g., Eberhardt et al., 2004). This paves the way for improved spatial and temporal modeling of both coseismic and post-seismic landslide occurrence and the next generation of path-dependent landslide susceptibility models (Korup & Stolle, 2014; Lombardo & Mai, 2018; Rodrigues et al., 2021; Samia et al., 2017a, 2017b). Less well developed, however, are numerical models of cracking processes and effects in rocks where static and dynamic stress fields interact (Burgers, 1980; Shao et al., 2006; Yang et al., 2014). As such, forecasting locations of path-dependent post-seismic behavior in field settings is likely to be initially based on empirical field and laboratory observations; our work provides first-order insight into the types of hillslopes most prone to path-dependent variations in mechanical properties. Our findings indicate that modeling of path-dependent hillslope response to ground shaking during the post-seismic phase must involve a range of strength scenarios beyond conventional "peak" and "residual" failure envelopes (Akin, 2013; Sonmez et al., 1998; Topal & Akin, 2009); model decisions on appropriate inputs for specific slope settings must be informed by factors including landslide depth, hillslope angle, the magnitude of accumulated strain and the nature of the seismic waveform experienced at that location. Future work must seek to integrate differences in the types of damage generated in different hillslope configurations and in response to ground shaking events of different character into predictive models of landslide behavior, and how this affects the evolution of both hillslopes and hazard in post-seismic landscapes. Such modeling will allow the spatial and temporal effects of path-dependent post-seismic landsliding to be assessed relative to a larger range of geomorphic processes (Chen et al., 2020; Croissant et al., 2019; Dahlquist & West, 2019; Hobley et al., 2017; Marc et al., 2019), providing more detailed insights into sub-regional spatial and temporal patterns of hillslope failure in the post-seismic phase (Fan et al., 2019; Kincey et al., 2021; Marc et al., 2015). In addition, ongoing laboratory testing must seek to explore the influence of varying states of saturation and pore-water pressure conditions on the static and dynamic behavior of hillslopes of varying lithology in response to differing baseline stress conditions and varying dynamic load amplitudes and frequencies.

6. Conclusions

Using geotechnical laboratory testing, we considered how the strength and rheology of rocks can vary in the post-seismic phase in response to dynamic loading that varies in character. Our results indicate that post-seismic hillslope strength can be unchanged, increased or decreased relative to pre-seismic conditions.

This path dependence is controlled by the amplitude of dynamic loading experienced at a particular location and the degree of pre-existing shear surface formation within hillslopes, which is in part a function of landslide depth and hillslope angle. These factors govern the nature and location of fractures and asperities along incipient shear surfaces, and whether or not these are subsequently mobilized and/or degraded during post-seismic shear. More intact rocks, akin to shallow landslides (depth, z, ≤5 m) in field settings, are most likely to display divergent, path-dependent changes to strength and rheology in the post-seismic phase in response to seismic loading events of different amplitude. In more developed shear surfaces typical of deeper landslides ($z \approx$ 20–30 m), dynamic loading is less likely to result in changes in post-seismic strength. However, dynamic loading causes enhanced asperity degradation, reducing the "critical strain" that landslides can sustain in the post-seismic phase. This has important implications for post-seismic assessment and forecasting of hillslope stability hazard.

Since the observed path dependence in hillslope behavior is a function of mechanisms common to brittle rocks, our findings are likely to be critical in a range of lithologies and seismic settings. In field locations, path-dependent behavior is likely to be manifest spatially in response to local to regional variations in landslide depth, hillslope angle and ground shaking intensity. Our findings add broader context and process understanding to regional scale datasets that consider the "recovery" of hillslope strength following earthquakes. Based on our results, and contrary to conclusions that may be drawn from synoptic regional-scale patterns, not all hillslopes will be more susceptible to failure in the post-seismic phase. Mechanisms of shear surface development and the specific nature of damage generated in different hillslope configurations and in response to ground shaking events of different character must be considered in assessments of post-seismic hillslope stability at a range of scales. Modeling path-dependent post-seismic hillslope behavior is an important next step in our ability to forecast how landscapes and landslide hazard evolve in the post-seismic phase over a range of spatial and temporal scales.

Conflict of Interest

The authors declare no conflicts of interest relevant to this study.

Data Availability Statement

Data considered in this paper are freely available from https://doi.org/10.5281/zenodo.5101461.

Acknowledgments
This work was funded by the RCUK/UKRI-Conicyt Newton Fund International Cooperation Programme Project NE/N000315/1 "Seismically induced landslides in Chile: New tools for hazard assessment and disaster prevention." The authors thank Bill Murphy and Melanie Froude for assistance with fieldwork and sampling, and Chris Longley for laboratory support. The authors are grateful to Odin Marc and two anonymous reviewers for their helpful and constructive comments on the initial draft of the manuscript.

References

Akin, M. (2013). Slope stability problems and back analysis in heavily jointed rock mass: A case study from manisa, Turkey. *Rock Mechanics and Rock Engineering*, *46*, 359–371. https://doi.org/10.1007/s00603-012-0262-x

Anderson, K., Westoby, M. J., & James, M. R. (2019). Low-budget topographic surveying comes of age: Structure from motion photogrammetry in geography and the geosciences. *Progress in Physical Geography: Earth and Environment*, *43*, 163–173. https://doi.org/10.1177/0309133319837454

Asadollahi, P., & Tonon, F. (2011). Degradation of rock fracture asperities in unloading, reloading, and reversal. *International Journal for Numerical and Analytical Methods in Geomechanics*, *35*, 1334–1346. https://doi.org/10.1002/nag.960

Attewell, P. B., & Farmer, I. W. (1976). *Principles of engineering geology*. London: Chapman and Hall.

Bahaaddini, M., Hagan, P. C., Mitra, R., & Khosravi, M. H. (2016). Experimental and numerical study of asperity degradation in the direct shear test. *Engineering Geology*, *204*, 41–52. https://doi.org/10.1016/j.enggeo.2016.01.018

Bahaaddini, M., Sharrock, G., & Hebblewhite, B. K. (2013). Numerical direct shear tests to model the shear behaviour of rock joints. *Computers and Geotechnics*, *51*, 101–115. https://doi.org/10.1016/j.compgeo.2013.02.003

Barbero, M., Barla, G., & Zaninetti, A. (1996). Dynamic shear strength of rock joints subjected to impulse loading. *International Journal of Rock Mechanics and Mining Sciences & Geomechanics*, *33*, 141–151. https://doi.org/10.1016/0148-9062(95)00049-6

Barla, G., Barla, M., Martinotti, M. E. (2010). Development of a new direct shear testing apparatus. *Rock Mechanics and Rock Engineering*, *43*, 117–122. https://doi.org/10.1007/s00603-009-0041-5

Barton, N. (1973). Review of a new shear-strength criterion for rock joints. *Engineering Geology*, *7*, 287–332. https://doi.org/10.1016/0013-7952(73)90013-6

Barton, N. (1976). The shear strength of rock and rock joints. *International Journal of Rock Mechanics and Mining Sciences*, *13*, 255–279. https://doi.org/10.1016/0148-9062(76)90003-6

Barton, N., & Choubey, V. (1977). The shear strength of rock joints in theory and practice. *Rock Mech. Felsmechanik Mécanique des Roches*, *10*, 1–54. https://doi.org/10.1007/BF01261801

Bekaert, D. P. S., Handwerger, A. L., Agram, P., & Kirschbaum, D. B. (2020). InSAR-based detection method for mapping and monitoring slow-moving landslides in remote regions with steep and mountainous terrain: An application to Nepal. *Remote Sensing of Environment*, *249*, 111983. https://doi.org/10.1016/j.rse.2020.111983

Belem, T., Souley, M., & Homand, F. (2007). Modeling surface roughness degradation of rock joint wall during monotonic and cyclic shearing. *Acta Geotech*, *2*, 227–248. https://doi.org/10.1007/s11440-007-0039-7

Bieniawski, Z. T. (1967). Mechanism of brittle fracture of rock: Part I—Theory of the fracture process. *International Journal of Rock Mechanics and Mining Science & Geomechanics Abstracts*, *4*, 395–406. https://doi.org/10.1016/0148-9062(67)90030-7

Bjerrum, L. (1967). Progressive failure in slopes of overconsolidated plastic clay and clay shales. *Proceedings of the American Society of Civil Engineers*, *93*, 5456.

Blott, S. J., & Pye, K. (2001). GRADISTAT: A grain size distribution and statistics package for the analysis of unconsolidated sediments. *Earth Surface Processes and Landforms*, *26*, 1237–1248. https://doi.org/10.1002/esp.261

Bontemps, N., Lacroix, P., Larose, E., Jara, J., & Taipe, E. (2020). Rain and small earthquakes maintain a slow-moving landslide in a persistent critical state. *Nature Communications*, *11*, 780. https://doi.org/10.1038/s41467-020-14445-3

Brain, M. J., Rosser, N. J., Norman, E. C., & Petley, D. N. (2014). Are microseismic ground displacements a significant geomorphic agent? *Geomorphology*, *207*, 161–173. https://doi.org/10.1016/j.geomorph.2013.11.002

Brain, M. J., Rosser, N. J., Sutton, J., Snelling, K., Tunstall, N., & Petley, D. N. (2015). The effects of normal and shear stress wave phasing on coseismic landslide displacement. *Journal of Geophysical Research: Earth Surface*, *120*, 1009–1022. https://doi.org/10.1002/2014JF003417

Brain, M. J., Rosser, N. J., & Tunstall, N. (2017). The control of earthquake sequences on hillslope stability. *Geophysical Research Letters*, *44*, 865–872. https://doi.org/10.1002/2016GL071879

Buech, F., Davies, T. R., & Pettinga, J. R. (2010). The little Red Hill seismic experimental study: Topographic effects on ground motion at a bedrock-dominated mountain edifice. *Bulletin of the Seismological Society of America*, *100*, 2219–2229. https://doi.org/10.1785/0120090345

Burgers, P. (1980). Dynamic linear elastic crack propagation in anti-plane shear by finite differences. *International Journal of Fracture*, *16*, 261–274. https://doi.org/10.1007/BF00013382

Burjánek, J., Moore, J. R., Yugsi Molina, F. X., & Fäh, D. (2012). Instrumental evidence of normal mode rock slope vibration. *Geophysical Journal International*, *188*, 559–569. https://doi.org/10.1111/j.1365-246X.2011.05272.x

Cai, M., Kaiser, P. K., Tasaka, Y., Maejima, T., Morioka, H., & Minami, M. (2004). Generalized crack initiation and crack damage stress thresholds of brittle rock masses near underground excavations. *International Journal of Rock Mechanics and Mining Sciences*, *41*, 833–847. https://doi.org/10.1016/j.ijrmms.2004.02.001

Carbonneau, P. E., & Dietrich, J. T. (2017). Cost-effective non-metric photogrammetry from consumer-grade sUAS: Implications for direct georeferencing of structure from motion photogrammetry. *Earth Surface Processes and Landforms*, *42*, 473–486. https://doi.org/10.1002/esp.4012

Carey, J. M., Cosgrove, B., Norton, K., Massey, C. I., Petley, D. N., & Lyndsell, B. (2021). Debris flow-slide initiation mechanisms in fill slopes, Wellington, New Zealand. *Landslides*, *18*, 1–12. https://doi.org/10.1007/s10346-021-01624-6

Carey, J. M., McSaveney, M. J., & Petley, D. N. (2017). Dynamic liquefaction of shear zones in intact loess during simulated earthquake loading. *Landslides*, *14*, 789–804. https://doi.org/10.1007/s10346-016-0746-y

Carter, M. R. (1990). Relative measures of soil bulk density to characterize compaction in tillage studies on fine sandy loams. *Canadian Journal of Soil Science*, *70*. https://doi.org/10.4141/cjss90-042

Chandler, R. J., & Skempton, A. W. (1974). The design of permanent cutting slopes in stiff fissured clays. *Géotechnique*, *24*, 457–466. https://doi.org/10.1680/geot.1974.24.4.457

Chen, M., Tang, C., Xiong, J., Shi, Q. Y., Li, N., Gong, L. F., et al. (2020). The long-term evolution of landslide activity near the epicentral area of the 2008 Wenchuan earthquake in China. *Geomorphology*, *367*, 107317. https://doi.org/10.1016/j.geomorph.2020.107317

Christakos, G. (2003). Soil behaviour under dynamic loading conditions: Experimental procedures and statistical trends. *Stochastic Environmental Research and Risk Assessment*, *17*, 175–190. https://doi.org/10.1007/s00477-003-0132-x

Clarke, B. A., & Burbank, D. W. (2011). Quantifying bedrock-fracture patterns within the shallow subsurface: Implications for rock mass strength, bedrock landslides, and erodibility. *Journal of Geophysical Research*, *116*, F04009. https://doi.org/10.1029/2011JF001987

Cooper, M. R., Bromhead, E. N., Petley, D. J., & Grants, D. I. (1998). The Selborne cutting stability experiment. *Géotechnique*, *48*, 83–101. https://doi.org/10.1680/geot.1998.48.1.83

Cresswell, A. W., & Barton, M. E. (2003). Direct shear tests on an uncemented, and a very slightly cemented, locked sand. *The Quarterly Journal of Engineering Geology and Hydrogeology*, *36*, 119–132. https://doi.org/10.1144/1470-923601-042

Croissant, T., Steer, P., Lague, D., Davy, P., Jeandet, L., & Hilton, R. G. (2019). Seismic cycles, earthquakes, landslides and sediment fluxes: Linking tectonics to surface processes using a reduced-complexity model. *Geomorphology*, *339*, 87–103. https://doi.org/10.1016/j.geomorph.2019.04.017

Dahlquist, M. P., & West, A. J. (2019). Initiation and runout of post-seismic debris flows: Insights from the 2015 Gorkha earthquake. *Geophysical Research Letters*, *46*, 9658–9668. https://doi.org/10.1029/2019GL083548

Delouis, B., Nocquet, J.-M., & Vallée, M. (2010). Slip distribution of the February 27, 2010 Mw = 8.8 Maule Earthquake, central Chile, from static and high-rate GPS, InSAR, and broadband teleseismic data. *Geophysical Research Letters*, *37*, L17305. https://doi.org/10.1029/2010GL043899

Dietze, M., Mohadjer, S., Turowski, J. M., Ehlers, T. A., & Hovius, N. (2017). Seismic monitoring of small alpine rockfalls – Validity, precision and limitations. *Earth SurfaceDynamics*, *5*, 653–668. https://doi.org/10.5194/esurf-5-653-2017

Dietze, M., Turowski, J. M., Cook, K. L., & Hovius, N. (2017). Spatiotemporal patterns, triggers and anatomies of seismically detected rockfalls. *Earth Surface Dynamics*, *5*, 757–779. https://doi.org/10.5194/esurf-5-757-2017

Dreyfus, D., Rathje, E. M., & Jibson, R. W. (2013). The influence of different simplified sliding-block models and input parameters on regional predictions of seismic landslides triggered by the Northridge earthquake. *Engineering Geology 163*, 41–54. https://doi.org/10.1016/j.enggeo.2013.05.015

Eberhardt, E., Stead, D., & Coggan, J. S. (2004). Numerical analysis of initiation and progressive failure in natural rock slopes-the 1991 Randa rockslide. *International Journal of Rock Mechanics and Mining Sciences*, *41*, 69–87. https://doi.org/10.1016/S1365-1609(03)00076-5

Eberhardt, E., Stead, D., Stimpson, B. (1999). Quantifying progressive pre-peak brittle fracture damage in rock during uniaxial compression. *International Journal of Rock Mechanics and Mining Sciences*, *36*, 361–380. https://doi.org/10.1016/S0148-9062(99)00019-4

Elnashai, A. S., Gencturk, B., Kwon, O.-S., Al-Qadi, I. L., Hashash, Y., Roesler, J. R., et al. (2010). The Maule (Chile) earthquake of February 27, 2010: Consequence assessment and case studies. In *Mid-America Earthquake Center*, Report No. 10–04. University of Illinois.

Erarslan, N. (2016). Microstructural investigation of subcritical crack propagation and fracture process zone (FPZ) by the reduction of rock fracture toughness under cyclic loading. *Engineering Geology*, *208*, 181–190. https://doi.org/10.1016/j.enggeo.2016.04.035

Escobar, F. T., Puig, A. G., & Muzzio, G. S. (1982). *Mapa Geológico de Chile (1:1,000,000)*. Santiago, Chile: Servicio Nacional de Geología y Minería.

Fan, X., Domènech, G., Scaringi, G., Huang, R., Xu, Q., Hales, T. C., et al. (2018). Spatio-temporal evolution of mass wasting after the 2008 Mw 7.9 Wenchuan earthquake revealed by a detailed multi-temporal inventory. *Landslides*, *15*, 2325–2341. https://doi.org/10.1007/s10346-018-1054-5

Fan, X., Scaringi, G., Korup, O., West, A. J., van Westen, C. J., Tanyas, H., et al. (2019). Earthquake-induced chains of geologic hazards: Patterns, mechanisms, and impacts. *Reviews of Geophysics*, *57*, 421–503. https://doi.org/10.1029/2018RG000626

Fathi, A., Moradian, Z., Rivard, P., & Ballivy, G. (2016). Shear mechanism of rock joints under pre-peak cyclic loading condition. *International Journal of Rock Mechanics and Mining Sciences*, *83*, 197–210. https://doi.org/10.1016/j.ijrmms.2016.01.009

Ferrero, A. M., Migliazza, M., & Tebaldi, G. (2010). Development of a new experimental apparatus for the study of the mechanical behaviour of a rock discontinuity under monotonic and cyclic loads. *Rock Mechanics and Rock Engineering*, *43*, 685–695. https://doi.org/10.1007/s00603-010-0111-8

Folk, R. L., & Ward, W. C. (1957). Brazos river bar [Texas]; a study in the significance of grain size parameters. *Journal of Sedimentary Research*, *27*, 3–26. https://doi.org/10.1306/74d70646-2b21-11d7-8648000102c1865d

Fonstad, M. A., Dietrich, J. T., Courville, B. C., Jensen, J. L., & Carbonneau, P. E. (2013). Topographic structure from motion: A new development in photogrammetric measurement. *Earth Surface Processes and Landforms*, *38*, 421–430. https://doi.org/10.1002/esp.3366

Franklin, J. A. (1985). Suggested method for determining point load strength. *International Journal of Rock Mechanics and Mining Sciences*, *22*, 51–60. https://doi.org/10.1016/0148-9062(85)92327-7

Gischig, V. S., Eberhardt, E., Moore, J. R., & Hungr, O. (2015). On the seismic response of deep-seated rock slope instabilities — Insights from numerical modeling. *Engineering Geology*, *193*, 1–18. https://doi.org/10.1016/j.enggeo.2015.04.003

Hackley, P. C., Warwick, P. D., Guillermo, A. H., & Rosenelsy, M. C. (2006). World coal quality inventory: Chile. In A. W. Karlsen, S. J. Tewalt, L. J. Bragg, & R. B. Finkelman (Eds.), *World coal quality inventory: South America*. United States Geological Survey.

Hadj-Hamou, T., & Kavazanjian, E. (1985). Seismic stability of gentle infinite slopes. *Journal of Geotechnical Engineering*, *111*, 681–697. https://doi.org/10.1061/(ASCE)0733-9410(1985)111:6(681)

Head, K. H. (2008). *Manual of soil laboratory testing volume one* (3rd ed.,). Caithness: Whittles Publishing.

Head, K. H., & Epps, R. J. (2011). *Manual of soil laboratory testing volume two: Permeability, shear strength and compressibility tests*. London: Taylor and Francis.

Head, K. H., & Epps, R. J. (2014). *Manual of soil laboratory testing volume 3: Effective stress tests* (3rd ed.,). Caithness: Whittles Publishing.

Heap, M. J., Baud, P., & Meredith, P. G. (2009). Influence of temperature on brittle creep in sandstones. *Geophysical Research Letters*, *36*, L19305. https://doi.org/10.1029/2009GL039373

Hernández-Gómez, L. H., Sauceda-Meza, I., Urriolagoitia-Calderön, G., Balankin, A. S., & Susarrey, O. (2004). Evaluation of crack initiation angle under mixed mode loading at diverse strain rates. *Theoretical and Applied Fracture Mechanics*, *42*, 53–61. https://doi.org/10.1016/j.tafmec.2004.06.008

Hobley, D. E. J., Adams, J. M., Siddhartha Nudurupati, S., Hutton, E. W. H., Gasparini, N. M., Istanbulluoglu, E., & Tucker, G. E. (2017). Creative computing with Landlab: An open-source toolkit for building, coupling, and exploring two-dimensional numerical models of Earth-surface dynamics. *Earth Surface Dynamics*, *5*, 21–46. https://doi.org/10.5194/esurf-5-21-2017

Hovius, N., Meunier, P., Lin, C.-W. W., Chen, H., Chen, Y.-G. G., Dadson, S., et al. (2011). Prolonged seismically induced erosion and the mass balance of a large earthquake. *Earth and Planetary Science Letters*, *304*, 347–355. https://doi.org/10.1016/j.epsl.2011.02.005

Hu, W., Scaringi, G., Xu, Q., & Huang, R. (2018). Internal erosion controls failure and runout of loose granular deposits: Evidence from flume tests and implications for postseismic slope healing. *Geophysical Research Letters*, *45*, 5518–5527. https://doi.org/10.1029/2018GL078030

Hutson, R. W., & Dowding, C. H. (1990). Joint asperity degradation during cyclic shear. *International Journal of Rock Mechanics and Mining Sciences*, *27*, 109–119. https://doi.org/10.1016/0148-9062(90)94859-R

ISRM. (1981). Basic geotechnical description of rock masses (BGD). *International Journal of Rock Mechanics and Mining Science & Geomechanics Abstracts*, *18*, 87–110. https://doi.org/10.1016/0148-9062(81)90277-1

Jacoby, G. C. (1997). Application of tree ring analysis to paleoseismology. *Reviews of Geophysics*, *35*, 109–124. https://doi.org/10.1029/96RG03526

Jaeger, J. C. (1971). Friction of rocks and stability of rock slopes. *Géotechnique*, *21*, 97–134. https://doi.org/10.1680/geot.1971.21.2.97

Jafari, M. K., Pellet, F., Boulon, M., & Hosseini, K. A. (2004). Experimental study of mechanical behaviour of rock joints under cyclic loading. *Rock Mechanics and Rock Engineering*, *37*, 3–23. https://doi.org/10.1007/s00603-003-0001-4

James, M. R., Chandler, J. H., Eltner, A., Fraser, C., Miller, P. E., Mills, J. P., et al. (2019). Guidelines on the use of structure-from-motion photogrammetry in geomorphic research. *Earth Surface Processes and Landforms*, *44*, 2081–2084. https://doi.org/10.1002/esp.4637

James, M. R., Robson, S., d'Oleire-Oltmanns, S., & Niethammer, U. (2017). Optimising UAV topographic surveys processed with structure-from-motion: Ground control quality, quantity and bundle adjustment. *Geomorphology*, *280*, 51–66. https://doi.org/10.1016/j.geomorph.2016.11.021

Jibson, R. W. (1993). Predicting earthquake-induced landslide displacements using Newmark's sliding block analysis. *Transportation Research Record 1411*, 9–17.

Jibson, R. W., Harp, E. L., & Michael, J. A. (2000). A method for producing digital probabilistic seismic landslide hazard maps. *Engineering Geology*, *58*, 271–289. https://doi.org/10.1016/S0013-7952(00)00039-9

Keefer, D. K. (1984). Landslides caused by earthquakes. *The Geological Society of America Bulletin*, *95*, 406–421. https://doi.org/10.1130/0016-7606(1984)95<406:lcbe>2.0.co;2

Kincey, M. E., Rosser, N. J., Robinson, T. R., Densmore, A. L., Shrestha, R., Pujara, D. S., et al. (2021). Evolution of coseismic and post-seismic landsliding after the 2015 M w 7.8 Gorkha earthquake, Nepal. *Journal of Geophysical Research: Earth Surface*, *126*, e2020JF005803. https://doi.org/10.1029/2020JF005803

Koi, T., Hotta, N., Ishigaki, I., Matuzaki, N., Uchiyama, Y., & Suzuki, M. (2008). Prolonged impact of earthquake-induced landslides on sediment yield in a mountain watershed: The Tanzawa region, Japan. *Geomorphology*, *101*, 692–702. https://doi.org/10.1016/j.geomorph.2008.03.007

Korup, O., & Stolle, A. (2014). Landslide prediction from machine learning. *Geology Today*, *30*, 26–33. https://doi.org/10.1111/gto.12034

Krsmanović, D. (1967). Initial and residual shear strength of hard rocks. *Géotechnique*, *17*, 145–160. https://doi.org/10.1680/geot.1967.17.2.145

Lacroix, P., Perfettini, H., Taipe, E., & Guillier, B. (2014). Coseismic and postseismic motion of a landslide: Observations, modeling, and analogy with tectonic faults. *Geophysical Research Letters*, *41*, 6676–6680. https://doi.org/10.1002/2014GL061170

Ladanyi, B., & Archambault, G. (1969). *Simulation of shear behavior of a jointed rock mass*.

Lajtai, E. Z. (1969a). Shear strength of weakness planes in rock. *International Journal of Rock Mechanics and Mining Sciences*, *6*, 499–515. https://doi.org/10.1016/0148-9062(69)90016-3

Lajtai, E. Z. (1969b). Strength of discontinuous rocks in direct shear. *Géotechnique*, *19*, 218–233. https://doi.org/10.1680/geot.1969.19.2.218
Lawrence, Z., Bodin, P., & Langston, C. A. (2009). In situ measurements of nonlinear and nonequilibrium dynamics in shallow, unconsolidated sediments. *Bulletin of the Seismological Society of America*, *99*, 1650–1670. https://doi.org/10.1785/0120080177
Lenti, L., & Martino, S. (2013). A parametric numerical study of the interaction between seismic waves and landslides for the evaluation of the susceptibility to seismically induced displacements. *Bulletin of the Seismological Society of America*, *103*, 33–56. https://doi.org/10.1785/0120120019
Leshchinsky, B., Lehmann, P., & Or, D. (2020). Enhanced rainfall-induced shallow landslide activity following seismic disturbance – From triggering to healing. *Journal of Geophysical Research: Earth Surface*, *126*, e2020JF005669. https://doi.org/10.1029/2020JF005669
Lin, G. W., Chen, H., Hovius, N., Horng, M. J., Dadson, S., Meunier, P., & Lines, M. (2008). Effects of earthquake and cyclone sequencing on landsliding and fluvial sediment transfer in a mountain catchment. *Earth Surface Processes and Landforms*, *33*, 1354–1373. https://doi.org/10.1002/esp.1716
Lombardo, L., & Mai, P. M. (2018). Presenting logistic regression-based landslide susceptibility results. *Engineering Geology*, *244*, 14–24. https://doi.org/10.1016/j.enggeo.2018.07.019
Lorito, S., Romano, F., Atzori, S., Tong, X., Avallone, A., McCloskey, J., et al. (2011). Limited overlap between the seismic gap and coseismic slip of the great 2010 Chile earthquake. *Nature Geoscience*, *4*, 173–177. https://doi.org/10.1038/ngeo1073
Lou, Y., Zhang, G., & Wang, X. (2019). Cracking mode analysis of crack initiation in rocks under uniaxial compression. *Advances in Civil Engineering*, *2019*, 1–9. https://doi.org/10.1155/2019/5818071
Malamud, B. D., Turcotte, D. L., Guzzetti, F., & Reichenbach, P. (2004). Landslides, earthquakes, and erosion. *Earth and Planetary Science Letters*, *229*, 45–59. https://doi.org/10.1016/j.epsl.2004.10.018
Marc, O., Behling, R., Andermann, C., Turowski, J. M., Illien, L., Roessner, S., & Hovius, N. (2019). Long-term erosion of the Nepal Himalayas by bedrock landsliding: The role of monsoons, earthquakes and giant landslides. *Earth Surface Dynamics*, *7*, 107–128. https://doi.org/10.5194/esurf-7-107-2019
Marc, O., Hovius, N., Meunier, P., Gorum, T., & Uchida, T. (2016). A seismologically consistent expression for the total area and volume of earthquake-triggered landsliding. *Journal of Geophysical Research: Earth Surface*, *121*, 640–663. https://doi.org/10.1002/2015JF003732
Marc, O., Hovius, N., Meunier, P., Uchida, T., & Hayashi, S. (2015). Transient changes of landslide rates after earthquakes. *Geology*, *43*, 883–886. https://doi.org/10.1130/G36961.1
Marc, O., Sens-Schönfelder, C., Illien, L., Meunier, P., Hobiger, M., Sawazaki, K., et al. (2021). Toward using seismic interferometry to quantify landscape mechanical variations after earthquakes. *Bulletin of the Seismological Society of America*, *111*, 1631–1649. https://doi.org/10.1785/0120200264
Martin, C. D., & Chandler, N. A. (1994). The progressive fracture of Lac du Bonnet granite. *International Journal of Rock Mechanics and Mining Science & Geomechanics Abstracts*, *31*, 643–659. https://doi.org/10.1016/0148-9062(94)90005-1
Melnick, D., Bookhagen, B., Strecker, M. R., & Echtler, H. P. (2009). Segmentation of megathrust rupture zones from fore-arc deformation patterns over hundreds to millions of years, Arauco peninsula, Chile. *Journal of Geophysical Research: Solid Earth*, *114*, B01407. https://doi.org/10.1029/2008JB005788
Meunier, P., Hovius, N., & Haines, A. J. (2007). Regional patterns of earthquake-triggered landslides and their relation to ground motion. *Geophysical Research Letters*, *34*, L20408. https://doi.org/10.1029/2007GL031337
Meunier, P., Hovius, N., & Haines, J. A. (2008). Topographic site effects and the location of earthquake induced landslides. *Earth and Planetary Science Letters*, *275*, 221–232. https://doi.org/10.1016/j.epsl.2008.07.020
Moore, J. R., Gischig, V., Burjanek, J., Loew, S., & Fäh, D. (2011). Site effects in unstable rock slopes: Dynamic behavior of the Randa instability (Switzerland). *Bulletin of the Seismological Society of America*, *101*, 3110–3116. https://doi.org/10.1785/0120110127
Munsell (2009). *Geological rock-color chart*. Grand Rapids, Michigan: Munsell.
Muralha, J., Grasselli, G., Tatone, B., Blümel, M., Chryssanthakis, P., & Yujing, J. (2014). ISRM suggested method for laboratory determination of the shear strength of rock joints: Revised version. *Rock Mechanics and Rock Engineering*, *47*, 291–302. https://doi.org/10.1007/s00603-013-0519-z
Newmark, N. M. (1965). Effects of earthquakes on dams and embankments. *Géotechnique*, *15*, 139–160.
Nielsen, S. N., & Valdovinos, C. (2008). Early pleistocene mollusks of the tubul formation, South-Central Chile. *Nautilus*, *122*, 201–216.
Nowicki Jessee, M. A., Hamburger, M. W., Ferrara, M. R., McLean, A., & FitzGerald, C. (2020). A global dataset and model of earthquake-induced landslide fatalities. *Landslides*, *17*, 1363–1376. https://doi.org/10.1007/s10346-020-01356-z
Parker, R. N., Densmore, A. L., Rosser, N. J., de Michele, M., Li, Y., Huang, R., et al. (2011). Mass wasting triggered by the 2008 Wenchuan earthquake is greater than orogenic growth. *Nature Geoscience*, *4*, 449–452. https://doi.org/10.1038/ngeo1154
Parker, R. N., Hancox, G. T., Petley, D. N., Massey, C. I., Densmore, A. L., & Rosser, N. J. (2015). Spatial distributions of earthquake-induced landslides and hillslope preconditioning in northwest South Island, New Zealand. *Earth Surface Dynamics Discussions*, *3*, 1–52. https://doi.org/10.5194/esurfd-3-1-2015
Patton, F. D. (1966). Multiple modes of shear failure in rock. In *Proceedings of the 1st ISRM congress* (pp. 509–513). Lisbon: Portugal.
Pereira, J. P., & de Freitas, M. H. (1993). Mechanisms of shear failure in artificial fractures of sandstone and their implication for models of hydromechanical coupling. *Rock Mechanics and Rock Engineering*, *26*, 195–214. https://doi.org/10.1007/BF01040115
Petley, D. N., & Allison, R. J. (1997). The mechanics of deep-seated landslides. *Earth Surface Processes and Landforms*, *22*, 747–758. https://doi.org/10.1002/(SICI)1096-9837(199708)22:8<747::AID-ESP767>3.0.CO;2-#
Petley, D. N., Higuchi, T., Petley, D. J., Bulmer, M. H., & Carey, J. (2005). Development of progressive landslide failure in cohesive materials. *Geology*, *33*, 201–204. https://doi.org/10.1130/g21147.1
Phillips, J. D. (2006). Evolutionary geomorphology: Thresholds and nonlinearity in landform response to environmental change. *Hydrology and Earth System Sciences*, *10*, 731–742. https://doi.org/10.5194/hess-10-731-2006
Qi, S., Zheng, B., Wu, F., Huang, X., Guo, S., Zhan, Z., et al. (2020). A new dynamic direct shear testing device on rock joints. *Rock Mechanics and Rock Engineering*, *53*, 4787–4798. https://doi.org/10.1007/s00603-020-02175-3
Rault, C., Chao, W., Gelis, C., Burtin, A., Chang, J., Marc, O., et al. (2020). Seismic response of a mountain ridge prone to landsliding. *Bulletin of the Seismological Society of America*, *110*, 3004–3020. https://doi.org/10.1785/0120190127
Roback, K., Clark, M. K., West, A. J., Zekkos, D., Li, G., Gallen, S. F., et al. (2018). The size, distribution, and mobility of landslides caused by the 2015 Mw7.8 Gorkha earthquake, Nepal. *Geomorphology*, *301*, 121–138. https://doi.org/10.1016/j.geomorph.2017.01.030
Robinson, T. R., Rosser, N. J., Davies, T. R. H., Wilson, T. M., & Orchiston, C. (2018). Near-real-time modeling of landslide impacts to inform rapid response: An example from the 2016 Kaikōura, New Zealand, earthquake. *Bulletin of the Seismological Society of America*, *108*, 1665–1682. https://doi.org/10.1785/0120170234

Rodrigues, S. G., Silva, M. M., & Alencar, M. H. (2021). A proposal for an approach to mapping susceptibility to landslides using natural language processing and machine learning. *Landslides*, *18*, 2515–2529. https://doi.org/10.1007/s10346-021-01643-3
Rodríguez, C. E., Bommer, J. J., & Chandler, R. J. (1999). Earthquake-induced landslides: 1980-1997. *Soil Dynamics and Earthquake Engineering*, *18*, 325–346. https://doi.org/10.1016/S0267-7261(99)00012-3
Rosser, N., Kincey, M., Oven, K., Densmore, A., Robinson, T., Pujara, D. S., et al. (2021). Changing significance of landslide hazard and risk after the 2015 Mw 7.8 Gorkha, Nepal earthquake. *Progress in Disaster Science*, *10*, 100159. https://doi.org/10.1016/j.pdisas.2021.100159
Rosser, N., Lim, M., Petley, D., Dunning, S., & Allison, R. (2007). Patterns of precursory rockfall prior to slope failure. *Journal of Geophysical Research: Earth Surface*, *112*, F04014. https://doi.org/10.1029/2006JF000642
Royán, M. J., Abellán, A., & Vilaplana, J. M. (2015). Progressive failure leading to the 3 December 2013 rockfall at Puigcercós scarp (Catalonia, Spain). *Landslides*, *12*, 585–595. https://doi.org/10.1007/s10346-015-0573-6
Saito, H., Uchiyama, S., Hayakawa, Y. S., & Obanawa, H. (2018). Landslides triggered by an earthquake and heavy rainfalls at Aso volcano, Japan, detected by UAS and SfM-MVS photogrammetry. *Progress in Earth and Planetary Science*, *5*, 15. https://doi.org/10.1186/s40645-018-0169-6
Salmon, M. W., Short, S. A., & Kennedy, R. P. (1992). *Strong motion duration and earthquake magnitude relationships*. California: Lawrence Livermore National Laboratory.
Samia, J., Temme, A., Bregt, A., Wallinga, J., Guzzetti, F., Ardizzone, F., & Rossi, M. (2017a). Characterization and quantification of path dependency in landslide susceptibility. *Geomorphology*, *292*, 16–24. https://doi.org/10.1016/j.geomorph.2017.04.039
Samia, J., Temme, A., Bregt, A., Wallinga, J., Guzzetti, F., Ardizzone, F., & Rossi, M. (2017b). Do landslides follow landslides? Insights in path dependency from a multi-temporal landslide inventory. *Landslides*, *14*, 547–558. https://doi.org/10.1007/s10346-016-0739-x
Selby, M. J. (1993). *Hillslope materials and processes*. Oxford: Oxford University Press.
Sepúlveda, S. A., Murphy, W., Jibson, R. W., Petley, D. N. (2005). Seismically induced rock slope failures resulting from topographic amplification of strong ground motions: The case of Pacoima Canyon, California. *Engineering Geology*, *80*, 336–348. https://doi.org/10.1016/j.enggeo.2005.07.004
Sepúlveda, S. A., Petley, D. N., Brain, M. J., & Tunstall, N. (2016). The effect of dynamic loading on the shear strength of pyroclastic ash deposits and implications for landslide hazard: The case of Pudahuel Ignimbrite, Chile. *Engineering Geology*, *205*, 54–61. https://doi.org/10.1016/j.enggeo.2016.02.005
Serey, A., Piñero-Feliciangeli, L., Sepúlveda, S. A., Poblete, F., Petley, D. N., & Murphy, W. (2019). Landslides induced by the 2010 Chile megathrust earthquake: A comprehensive inventory and correlations with geological and seismic factors. *Landslides*, *16*, 1153–1165. https://doi.org/10.1007/s10346-019-01150-6
Shao, P., Zhang, Y., Gao, W. M., & Liu, Y. Q. (2006). Dynamic response of intermittent jointed rock mass subjected to blast waves. *Key Engineering Materials*, *306–308*, 1415–1420. https://doi.org/10.4028/www.scientific.net/kem.306-308.1415
Sonmez, H., Ulusay, R., & Gokceoglu, C. (1998). A practical procedure for the back analysis of slope failures in closely jointed rock masses. *International Journal of Rock Mechanics and Mining Sciences*, *35*, 219–233. https://doi.org/10.1016/S0148-9062(97)00335-5
Stead, D., & Wolter, A. (2015). A critical review of rock slope failure mechanisms: The importance of structural geology. *Journal of Structural Geology*. https://doi.org/10.1016/j.jsg.2015.02.002
Swirad, Z. M., Rosser, N. J., & Brain, M. J. (2019). Identifying mechanisms of shore platform erosion using Structure-from-Motion (SfM) photogrammetry. *Earth Surface Processes and Landforms*, *44*, 1542–1558. https://doi.org/10.1002/esp.4591
Tanyaş, H., van Westen, C. J., Allstadt, K. E., Anna Nowicki Jessee, M., Görüm, T., Jibson, R. W., et al. (2017). Presentation and analysis of a worldwide database of earthquake-induced landslide inventories. *Journal of Geophysical Research: Earth Surface*, *122*, 1991–2015. https://doi.org/10.1002/2017JF004236
Temme, A. J. A. M., Keiler, M., Karssenberg, D., & Lang, A. (2015). Complexity and non-linearity in earth surface processes - Concepts, methods and applications. *Earth Surface Processes and Landforms*, *40*, 1270–1274. https://doi.org/10.1002/esp.3712
Topal, T., & Akin, M. (2009). Geotechnical assessment of a landslide along a natural gas pipeline for possible remediations (Karacabey-Turkey). *Environmental Geology*, *57*, 611–620. https://doi.org/10.1007/s00254-008-1330-0
Trifunac, M. D., & Brady, A. G. (1975). A study on the duration of strong earthquake ground motion. *Bulletin of the Seismological Society of America*, *65*, 581–626.
Verdugo, R., Villalobos, F., Yasuda, S., Konagai, K., Sugano, T., Okamura, M., et al. (2010). Description and analysis of geotechnical aspects associated to the large 2010 Chile earthquake. *Obras y Proyectos*, *8*, 27–33.
Viles, H., Messenzehl, K., Mayaud, J., Coombes, M., & Bourke, M. (2018). Stress histories control rock-breakdown trajectories in arid environments. *Geology*, *46*, 419–422. https://doi.org/10.1130/G39637.1
Vinciguerra, S., Trovato, C., Meredith, P. G., & Benson, P. M. (2005). Relating seismic velocities, thermal cracking and permeability in Mt. Etna and Iceland basalts. *International Journal of Rock Mechanics and Mining Sciences*, *42*, 900–910. https://doi.org/10.1016/j.ijrmms.2005.05.022
Wang, J., Jin, Z., Hilton, R. G., Zhang, F., Densmore, A. L., Li, G., & West, A. J. (2015). Controls on fluvial evacuation of sediment from earthquake-triggered landslides. *Geology*, *43*, 115–118. https://doi.org/10.1130/G36157.1
Whalley, W. B. (1991). Material properties. In A. S., Goudie, M., Anderson, T., Burt, J., Lewin, K., Richards, B., Whalley, P., Worsley (Eds.), *Geomorphological techniques* (pp. 169–185). London: Routledge. https://doi.org/10.4324/9780203430590
Williams, J. G., Rosser, N. J., Hardy, R. J., & Brain, M. J. (2019). The importance of monitoring interval for rockfall magnitude-frequency estimation. *Journal of Geophysical Research: Earth Surface*, *124*, 2841–2853. https://doi.org/10.1029/2019JF005225
Wyllie, D. C. (1999). *Foundations on rock* (2nd ed.,). Abingdon, Oxon: Spon Press/Taylor and Francis Group.
Yamasaki, S., Chigira, M., & Petley, D. N. (2016). The role of graphite layers in gravitational deformation of pelitic schist. *Engineering Geology*, *208*, 29–38. https://doi.org/10.1016/j.enggeo.2016.04.018
Yang, L., Yang, R., Qu, G., & Zhang, Y. (2014). Caustic study on blast-induced wing crack behaviors in dynamic-static superimposed stress field. *International Journal of Mining Science and Technology*, *24*, 417–423. https://doi.org/10.1016/j.ijmst.2014.05.001
Yin, Z., Liu, X., Yang, Z., Jiang, Y., Zhao, Y., & Li, S. (2020). Shear characteristics and failure mode of hard Brittle Marl with parallel discontinuous structural plane. *Arabian Journal for Science and Engineering*, *45*, 8219–8229. https://doi.org/10.1007/s13369-020-04674-5
Yunus, A. P., Fan, X., Tang, X., Jie, D., Xu, Q., & Huang, R. (2020). Decadal vegetation succession from MODIS reveals the spatio-temporal evolution of post-seismic landsliding after the 2008 Wenchuan earthquake. *Remote Sensing of Environment*, *236*, 111476. https://doi.org/10.1016/j.rse.2019.111476
Zhang, S., Zhang, L., Lacasse, S., & Nadim, F. (2016). Evolution of mass movements near epicentre of Wenchuan Earthquake, the first eight years. *Scientific Reports*, *6*, 1–9. https://doi.org/10.1038/srep36154